UNIVERSIDAD NACIONAL AUTÓNOMA DE MÉXICO

Posgrado en Ciencia e Ingeniería de Materiales

Instituto de Investigaciones en Materiales

Nonlinear optical properties of nanocolloids

T E S I S

Que para optar por el grado de :

Doctora en Ciencia e Ingeniería de Materiales

P R E S E N T A:

M.C. Martha Yadira Salazar Romero

Tutor: Dr. Juan A. Hernández Cordero
Instituto de Investigaciones en Materiales, UNAM

Co-Tutor: Dra. Karen P. Volke Sepúlveda
Instituto de Física, UNAM

Comité Tutor: Dr. Antonmaría Minzoni Alessio[†]
Instituto de Investigaciones en Matemáticas Aplicadas y Sistemas,
UNAM

Comité Tutor: Dr. Alejandro Vásquez Arzola
Instituto de Física, UNAM

Ciudad Universitaria. Enero 2019

Jurado

Presidente
Dr. Stephen Muhl Saunders
Instituto de Investigaciones en Materiales, UNAM.

Primer Vocal
Dra Karen Patricia Volke Sepúlveda
Instituto de Física, UNAM.

Segundo Vocal
Dr. Tupak García Fernández
Instituto de Ciencias Aplicadas y Tecnología, UNAM.

Tercer Vocal
Dr. Augusto García Valenzuela
Instituto de Ciencias Aplicadas y Tecnología, UNAM.

Secretario
Dr. Mathieu Christian Anne Hautefeuille
Facultad de Ciencias, UNAM.

Agradecimientos

La realización de esta tesis nunca habría sido posible sin el apoyo de las personas que me rodean, principalmente aquellas que siempre me brindan su cariño sincero. Espero no olvidar a nadie en los agradecimientos que a continuación daré, pero si lees este trabajo y me conociste alguna vez, ten por seguro que también a tí tengo algo qué agradecerte.

Quiero agradecer a mis tutores por todo su apoyo, paciencia y esfuerzo. A la Dra. Karen Volke por compartir conmigo su conocimiento, su bondad y alegría. Al Dr. Juan Hernández por permitirme trabajar tantos años con él, por su comprensión y ayuda. Al Dr. Alejandro Vásquez por su ayuda en el laboratorio, por ser tan amable y comprensivo. Al Dr. Tim Minzoni por compartir su inmensa sabiduria conmigo. También agtradezco las observaciones de todos mis sinodales, los doctores Augusto Valenzuela, Tupack García, Mathieu Hautefeuille y Stephen Muhl.

A mis padres Silvia Romero y Francisco Salazar, por su infinito amor incondicional, su comprensión y compañía durante toda mi vida. Mis hermanos, Hugo y Paco, gracias por ser un ejemplo de perseverancia, disciplina, constancia y pasión, yo jamás podría haber logrado nada en mi vida sin su compañía.

Gracias a toda mi familia, mis tios, primos y nuevos integrantes, principalmente a mis tios Reyna, Carlos, Armando, Gaby y Vicky por acompañarme y respetarme siempre. A mis primos Julio, Manuel, Karlita, Estrella y Regina, por existir, quererme y compartir sus gustos, disgustos, angustias, risas y todo lo que comparten conmigo.

A todos mis amigos (aquí la lista es larga porque soy como un gitano) muy especialmente a Estrella Terán porque sin su compañía, cariño y apoyo nunca habría

podido avanzar en la escritura de esta tesis, eres una amiga en toda la extensión de la palabra y le agradezco a la vida, al universo y a Dios que me permitió conocerte y tener el privilegio de caerte bien. A Memo Mungía, por ser mi confidente, amigo, protector y todo lo que el sabe que es para mí. A Roxana y a Victor por darme fuerza a través de su ejemplo, por su forma de afrontar la vida y las dificultades que siempre surgen en ella. A Renato y a Raúl por ser una guía, por brindarme su cariño sincero y sus sabias palabras en todos los momentos de mi vida desde que los conozco. A Vladimir Lemus por ser implacable y compartir su sabiduría conmigo. A Hans porque es un ejemplo de paciencia y perseverancia, por ser ese genio a quien admiro y quiero. A Lucía Cabriales por compartirme su alegría, dedicación, por su comprensión y amor. A Argelia por su compañia por escucharme siempre en las cenas largas. A Ceci y Andrea porque llegaron a mi vida para quedarse siempre como dos hermanas que no tuve, pero que, la vida me regaló. A Ana Laura por ser como quiere ser siempre. A Enrique por ser mi compañero de fiesta, por ser una persona honesta, sincera y cariñosa. A Adrian Bartolo por ser tan buen amigo y por quererme mucho, por dejarme compartir con él y su familia todo lo que juntos vivimos.

Al nuevo grupo de amigos que llegaron durante el proceso de escritura de esta tesis y que pasaron conmigo toda la frustración y sufrimiento, pero también todo lo bueno que de esto surgió. Mitzy, Dennisse y Marisol, por los cafés de mitad de semana por escuchar y compartir nuestras aventuras. Izamar por su alegría y por contagiarme de su juventud por introducir a mi vida a otras jóvenes y buenas personas. A Gustavo, Memo y Juanito por su ternura, amabilidad y sinceridad. A Jorge por esas tardes de carrera en C.U., por ser una de las personas que me hacen tener fé en la bondad del hombre.

Quiero dar un agradecimiento muy especial y sincero a una persona que hizo que mi sosciego huyera, que me despertó y que me acompaña en una nueva codificación del presente pero que muy seguramente estará en mi futuro de una manera única. Gracias por aparecer, por tu compañía, amor, amistad y todo lo que me brindas Gabriel Mercado Vásquez. De no haberte conocido, seguramente habría acabado mi tesis antes, pero no habría aprendido lo que sé ahora.

Contents

List of Figures

Abstract

The nonlinear optical properties of different samples of dielectric nanocolloids and their application to generate optical spatial solitons (OSS) in two transverse dimensions are investigated. We analyze four dielectric nanocolloids constituted by polystyrene nanospheres suspended in water, using two particle sizes (62 nm and 77 nm-diameter) and two concentrations ($C = 0.5\%$ and $C = 1.0\%$ of solids). All the studied samples exhibit positive polarizability, meaning that the refractive index of the nanoparticles is larger than that of the medium. The Z-scan technique was used to evaluate (qualitatively) and compare the nonlinear refractive index of the nanocolloids.

The OSS propagation formation in dielectric nanocolloid is demonstrated for distances of up to 10 mm, which is an unexpectedly long in comparison with previous works [1,2]. A detailed experimental study on the formation of solitons as a function of parameters, such as power (P), distance between focusing lens and the sample container (D), is also presented. Next, the nonlinear effects of light propagation through a fluorescent nanocolloid, where optical spatial solitons are also formed, are studied. The medium is constituted by a mixture of a transparent and fluorescent and nanoparticles in water. The conditions to create optical spatial solitons are analyzed as a function of the incident power. When the power is continuously change,

some evidence of a hysteresis effect is observed for the size of the transversal sections of the output beam. Other effects associated to the presence of the fluorescent nanospheres, such as an asymmetric ring pattern around the resulting OSS which appear at high input power are also discussed.

Different regimes for incoherent interactions between two orthogonally-polarized solitons in a colloidal suspension of nanoparticles with positive polarizability were unveiled. Even though the interaction is always attractive, it noticeably changes as a function of the ratio of power between the input beams and theangle between them. For interaction angles smaller than 10°, both interacting solitons fuse into a single entity, whose angle of propagation can be continuously steered. As the interaction angle increases, the resulting soliton can be practically switched between two positions when the power balance between the beams is changed. For interaction angles larger than 10° the result is no longer a single emerging soliton when the input power is equally distributed between the two beams. Moreover, the relative angle between the output beams is smaller than the angle between the input beams, meaning that there is still a kind of attractive interaction between them. When the power imbalance exceeds 12%, a single soliton starts forming again, propagating with almost the same direction as the highest intensity input beam.

Resumen

En esta tesis se investigan las propiedades ópticas no lineales de diferentes muestras de nanocoloides dieléctricos y su aplicación para generar solitones ópticos espaciales con dos dimensiones transversales.

Todas las muestras que se investigan exhiben polarizabilidad positiva, esto significa que el índice de refracción de las partículas es mayor que el del medio en que están inmersas. Se analizan cuatro muestras constituidas por nanoesferas de poliestireno suspendidas en agua, usando dos tamaños de partículas diferentes ($62nm$, $77nm$ de diámetro) y dos concentraciones (0.5% y 1.0% de sólidos respectivamente). Se implementa la técnica de Z-scan, con el fin de evaluar (cualitativamente) y comparar el índice de refracción no lineal de las suspensiones coloidales.

Demostramos que se pueden producir solitones ópticos espaciales estable con longitudes de propagación de más de 10 mm, la cual es inesperadamente larga en comparación con otros trabajos [1, 2]. También se presenta un tudio detallado sobre la formación de solitones como función de diferentes parámetros experimentales como la potencia P y la distancia entre la lente enfocante y el contenedor de la muestra. Por otro lado, se estudian los efectos no lineales de la propagación de la luz a través de de un coloide formado por una mezcla de pattículas transparentes y

fluorescentes, donde también se forman solitones opticos espaciales. En este caso, los medios están constituidos por una suspensión bidispersa de nanopartículas fluorescentes y no fluorescentes suspendidas en agua destilada. Las condiciones de enfoque para crear solitones ópticos espaciales se analizan como una función de la potencia incidente. Se observan indicios de histéresis para el tamaño del haz de salida, cuando la potencia aumenta y disminuye continuamente. También se discuten otros efectos asociados a la presencia de las nanoesferas fluorescentes, por ejemplo, la formación de un patrón asimétrico de anillos, que aparece con potencias altas del haz de entrada.

Posteriormente, se presentan diferentes regímenes para las interacciones incoherentes entre dos solitones con polarizaciones ortogonales en una suspensión coloidal de nanopartículas con polarizabilidad positiva. Aunque la interacción siempre es atractiva, cambia notablemente como función de la potencia relativa entre los dos haces y el ángulo entre ellos. Para pequeños ángulos, ambos solitones se fusionan en uno solo, su ángulo de propagación puede ser dirigido de forma continua. A medida que aumenta el ángulo de interacción, el solitón resultante puede saltar (switching) prácticamente entre dos posiciones cuando se altera el equilibrio de potencia entre los rayos. Por útlimo, para ángulos de interacción mayores a 10° el resultado es un solo solitón emergente cuando la potencia de entrada entre los dos rayos se distribuye aproximadamente igual. El ángulo relativo entre los rayos de salida es más pequeño que el ángulo entre los haces de entrada, lo que significa que continua habiendo interacción atractiva entre ellos. Cuando el desequilibrio de potencia supera 12%, comienza a formarse un solo solitón de nuevo, propagándose casi con la misma dirección del haz de entrada que tiene mayor potencia.

Introduction

The simplest classification of matter includes solids, liquids and gases [3]. However, some artificial materials do not necessarily fall within this categorization. These include colloids, polymers and liquid crystals [3]. The structure and properties of such materials have been characterized by theoretical and experimental techniques. As an example, studies on the interactions between light and these materials have led to the understanding of nonlinear optical effects, which in turn have contributed to the field of nonlinear optics [4–9].

Nonlinear optics emerged with the laser invention in the $1960s$ [5, 10, 11], when it was observed that materials properties depend of the intensity of the incident light [5,6]. Light-matter interaction is described through the polarization vector $\vec{P}$, which relates the material properties and the electric field $\vec{E}$ of light [5,6,10–12] as:

$$P(t) = \chi^{(1)} E(t) + \chi^{(2)} E^{(2)}(t) + \chi^{(3)} E^{(3)}(t) + ... \tag{1}$$

The first term corresponds to the linear regime, whereas the higher order terms are used for the nonlinear regime. These nonlinear terms lead to a number of very interesting effects that have attracted a lot of attention for technological and scien-

tific applications. In particular, we will focus on phenomena that occur in materials in which the third term of the above expression predominates [13]. Such materials exhibit relevant nonlinear optical effects, that allow the formation of optical solitons [5–7, 10–13].

Solitons or solitary waves arise when linear and nonlinear effects compensate each other leading to a wave that remains unchanged on propagation. These have been the subject of intense theoretical and experimental studies in many different fields such as hydrodynamics, optics and plasma physics, among others [14, 15]. Solitons can be either temporal or spatial [7, 14]. In optics, the first case refers to light pulses that preserve their shape without dispersion, which is compensated by the nonlinear effect of self-phase modulation. Optical spatial soliton (OSS) which is one of the main subjects of this thesis, results from the compensation of diffraction and the self-focusing effect [1, 14–16]. Both types of nonlinear effects, self-phase modulation and self-focusing, appear due to an intensity dependence of the refractive index [6, 7, 11, 14, 15]. If the dependence is simply linear, the material is known as a Kerr medium. When the refractive index is a more complicated function of the intensity the materials are referred to as Kerr-like.

In Kerr media OSS can only be induced in one dimension in the transverse plane, whereas many Kerr-like materials support solitons with a two-dimensional transverse profile. These cases are denoted as (1+1)D and (2+1)D, respectively, referring to the transverse coordinates and the propagation variable. Solitons in (2+1)D in Kerr media are precluded due to a catastrophic collapse, meaning that the self-focusing effect dominates over diffraction. However, the formation of OSS in (2+1)D has been

extensively studied in a variety of nonlinear materials such as photorefractive crystals [17] and nematic liquid crystals (NLC) [18]. For example, NLC are anisotropic materials composed by organic molecules with a permanent electric dipole that exhibit a nonlinearity as a consequence of molecular reorientation in response to an external electric field. For this reason, they are sensitive to the light polarization [18]. The OSS formed in NLC are called nematicons [19].

Other materials such as colloidal suspensions have also been studied for OSS propagation. A colloidal suspension is an artificial nonlinear optical material formed by tiny discrete components (typically particles) with sizes ranging from 10^{-9} m to 10^{-6} m, suspended in a liquid continuum phase [20–22]. The nonlinear optical properties and the propagation of OSS in these media were first reported in 1982 [1, 23–25]. In reference [1], colloidal samples of polystyrene nanospheres suspended in water, with radii ranging from 38 nm to 234 nm, were analyzed in order to determine the relevant experimental parameters involved in OSS formation, such as the minimum optical power required for the formation of the soliton. The maximum propagation distances of the OSS reached up to 600 μm in the highly scattering medium.

Recent progress in the synthesis capabilities and applications of different kinds of nanoparticles has renewed the interest in these materials for nonlinear optical applications [2, 26].

The nonlinear optical response of dielectric nanocolloidal suspensions is attributed to the gradient optical force, which attracts (repeals) dielectric particles towards (away from) the region of maximum light intensity, if their refractive index is higher

(lower) than that of the surrounding medium [23]. In the case of a colloid, this causes the particles to rearrange following the spatial variations of the light intensity. These variations appear, for instance, in a beam with a Gaussian transverse profile [1, 23–25]. The nanoparticle redistribution is generally described in terms of the electric polarizability (α) whose sign is determined by the refractive indices of the particles n_p and the background n_b. When the particle refractive index is higher than the refractive index of the background ($n_p > n_b$), the polarizability is positive ($\alpha > 0$). Under these conditions, the nanoparticles are accumulated in the regions of highest intensity and increases the local refractive index. If $n_p < n_b$, then $\alpha < 0$ and the nanoparticles are expelled from the regions of maximum intensity. Self-transparency arises due to the depletion of particles from the beam path [2]. In both cases, the redistribution of particles gives rise to a gradient in the effective refractive index of the medium, which produces a self-focusing effect.

In the context of OSS, particles with $\alpha < 0$ give rise to larger propagation distances than those reached by a beam traversing a colloid with particles with $\alpha > 0$ [2]. Indeed, OSS with propagation distances of a few millimeters have been observed in specially tailored media with $\alpha < 0$. This would be totally unexpected for media with $\alpha > 0$ [2, 26]. More recently, other nanosuspensions, made with metallic particles, have also been used to produce OSS with propagation distances of several millimeters, assisted by plasmonic resonances. [26].

Several theoretical models have been developed to describe the nonlinear response of dielectric colloidal media [16, 24, 27–30]. Different considerations and assumptions have been made in order to describe the nonlinearity of nanocolloids. In the simplest

model, an ideal gas of noninteracting spheres is considered, giving rise to a nonlinearity that varies exponentially with the optical intensity [16]. Stable solitons can be obtained in (1+1)D in this case, but not in (2+1)D. However, when other relevant effects are included, such as nonlinear losses due to Rayleigh scattering, this can lead to the formation of stable solitons in (2+1)D [28]. The incorporation of particle interactions as hard-sphere potential [31], or Coulomb repulsion forces [30], also lead to OSS solutions in (2+1)D. Although successful qualitative comparisons between theory and experiments have been attained with these models, a full quantitative comparison is still an active research topic [24, 26, 32].

In terms of applications, OSS are very appealing because they can create waveguides for a probe beam [7, 8, 33]. This might be relevant for dynamic data transmission, since it would be possible to carry information through optical beams with specific paths. In this case, rerouting and/or redirecting the OSS becomes an utterly important target, which has been pursued with different approaches. For example, steering of nematicons has been achieved through electric fields [34, 35], or through the interaction with additional light beams [36, 37]. Other media such as photorefractive crystals have been explored as an alternative for OSS routing through beam interactions [15, 38–41]. However, the response time of both of these materials, is not considered suitable for data transmission standards. In the case of photorefractive crystals the values are of the order of $\cong 10^2$ s [17, 38, 42] and for NLC are of the order of 25 s [18]. In contrast, as we will expose later, the response time of dielectric nanocolloids for OSS formation is one order of magnitude faster than NLC. Indeed, they have a response time of the order of 1 s.

The response time of colloidal suspensions is an advantage for rerouting and also for studies of other effects as interactions of OSS. The interactions between OSS in colloids have also been investigated: numerical work with (1+1)D OSS in colloids containing particles with $\alpha > 0$ [43], and (2+1)D OSS in colloids with mixtures of nanoparticles with $\alpha > 0$ and $\alpha < 0$ [31], has shown that interesting effects occur owing to OSS interaction. Experimentally, interactions between (2+1)D OSS in a nanocolloid with $\alpha < 0$ has also been studied, showing that OSS can attract or repel one another, depending on the launching conditions of the beams, such as their relative phases [44]. Soliton interactions in nanocolloids with $\alpha > 0$ have been considered to be unfeasible due to the catastrophic collapse during propagation predicted by the theoretical models [2, 44]. Although these studies about nanocolloids with $\alpha > 0$, in a previous work, the use of OSS as a waveguide and the observations of propagation distances along more than 1 mm [8] have been observed. These observations opened the motivation of this work, which relies on the interest of studying the nonlinear optical response of dielectric nanocolloidal suspensions through OSS formation and propagation. Additionally, the question that if it is possible that the waveguide conditions may provide a way to guide fluorescence signals generated by fluorescent particle contained within the colloid.

Accordingly, the objectives of this thesis are:

- Investigate experimentally the nonlinear response of dielectric nanocolloids with $\alpha > 0$.

- Identify and characterize in detail, the relevant experimental parameters for

the formation and propagation of optical spatial solitons OSS.

- Study the OSS behavior under different experimental conditions including concentration and particle size.

- Evaluate the possibility to guide fluorescence light using soliton-induced waveguides in dielectric nanocolloids.

- Explore the interactions between two solitons launched into nanocolloids with positive polarizability.

This work is organized as follows: in the first chapter, we will present the basic concepts, including a description of nanocolloids, and sample characterization techniques such as Z-scan and ultraviolet-visible absorption analysis (UV-vis). We will present also a brief description of the Kerr effect and the formation of OSS in these media. The second chapter includes results of studying the formation and propagation of OSS in the dielectric nanocolloids with positive polarizability, pointing out the relevant control parameters. In the third chapter, we will investigate the effects of using fluorescent particles in the formation of OSS. The fourth chapter includes results on the interaction of two solitons that impinge on the colloidal sample under different launching conditions. Finally, the last chapter includes the conclusions of this work.

Basic concepts

This chapter covers the basic concepts supporting this thesis. First, a short introduction about colloidal suspensions is provided. Then, the principles behind a linear optical characterization technique, namely UV-VIS spectroscopy, are presented. We will cover the relevant effects involved in optical spatial solitons formation, such as the optical Kerr effect and the self-focusing phenomenon. After that, Z-scan technique used for nonlinear optical characterization is described. Because of their fundamental role in nonlinear properties of colloidal media, the optical forces on these materials are also explained.

1.1 Colloidal suspensions

Colloids are typically described as media composed by two materials with different phases and their basic features and applications have been a research topic since the early 1940s [20]. One of the phases is known as the continuous phase (denoted

as A), which can be a soft solid or a fluid. The other one is called the dispersed phase (denoted as B), which is composed typically by particles of a size ranging from 10^{-9} m to 10^{-6} m [20, 21]. The molecules of the continuous phase must be significantly smaller than the dispersed particles phase B, which can be considered continuum (see Fig. 1.1). Phase A can be characterized by properties such as viscosity, dielectric constant and refractive index [21].
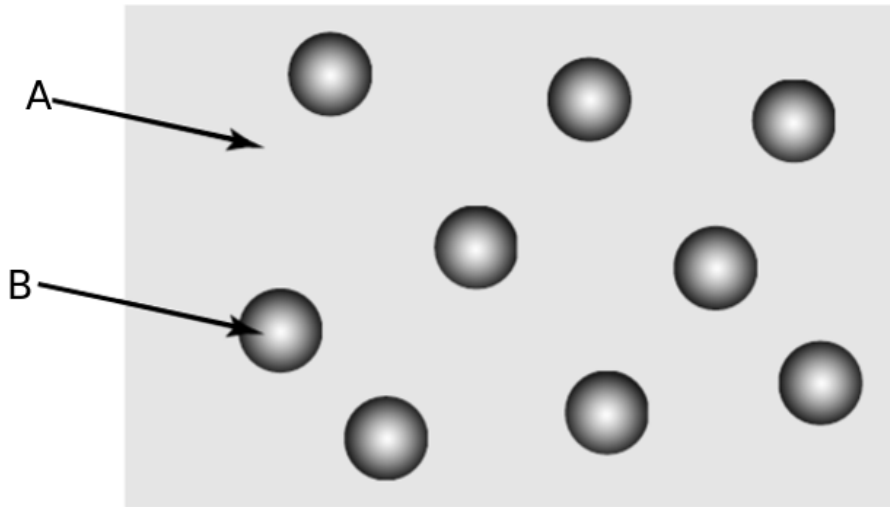
Figure 1.1: Typical colloidal system illustrating the continuum phase A and the dispersed phase B [45].

If A is a liquid and the dispersed phase B does not form a sediment, the colloid is said to be stable [22]. Several examples of colloids can be found in daily life, such as gels, emulsions, foods, biological systems like blood, and coatings are shown in table 1.1.

Colloidal particles are characterized by their Brownian motion, which comes from the thermal energy $k_B T$, where k_B is the Boltzmann constant and T is the absolute temperature [22]. Particles have also a characteristic diffusion coefficient given by:

Phases		
Dispersed	**Continuous**	**System Name**
Liquid	Gas	Aerosol fog, spray
Gas	Liquid	Foam, thin films, froth
		Fire extinguisher foam
Liquid	Liquid	Emulsion (milk)
		Mayonnaise, butter
Solid	Liquid	Sols, AgI, photography films
		Suspension wastewater
		Cement
		Oil recovery (shale oil)
		Coal slurry
Bio colloids		
Corpuscles	Serum	Blood
		Blood-coagulants
Hydroxyapatite	Collagen	Bone–teeth
Liquid	Solid	Solid emulsion (toothpaste; paints)
Solid	Gas	Solid aerosol (dust)
Gas	Solid	Solid foam (polystyrene)
		Insulating foam
Solid	Solid	Solid suspension/solids in plastics

Table 1.1: Examples of colloids [3].

$$D = \frac{\langle x^2 \rangle}{6\tau}, \tag{1.1}$$

where $\langle x^2 \rangle$ is the mean square distance between particles and τ is the mean time that a particle takes to diffuse a distance equal to its radius [22]. For dilute colloidal suspensions, body forces such as gravity, mechanical or thermal convection are not considered. The diffusion coefficient D for spherical particles is given by the ratio of the thermal energy $k_B T$ and the frictional Stokes drag force f,

$$D = \frac{k_B T}{f}; \tag{1.2}$$

$$f = 6\pi\eta_0 a, \tag{1.3}$$

where η_0 is the solvent viscosity and a is the particle radius. In general, the square of the particle radius (a^2) can be considered to be proportional to the mean square distance $(\langle x^2 \rangle)$ *i.e.*, $(\langle x^2 \rangle \propto a^2)$ and the characteristic time scale for a colloid can be therefore defined as:

$$\tau = \frac{\pi\eta_0 a^3}{k_B T}. \tag{1.4}$$

Another important characteristic of colloids is their concentration, which can be defined in different ways. In particular, a commonly used definition is:

$$\phi = nv_p = n(\frac{4}{3}\pi a^3), \tag{1.5}$$

where v_p is the volume of a particle and

$$n = \frac{N}{V}, \tag{1.6}$$

where N is the number of particles per unit volume V. Note that equation 1.5 is only valid for spherical, monodisperse (monomodal size distribution) particles.

In general colloids have particles with different sizes, the term size is concern to the

diameter d of the particles rather than the radius a. Colloids can be monomodal, that is, have a well-defined mean particle size but have a spread of particle sizes around a modal value, which means that they have certain degree of polydispersity. The modal value is the size that occurs more frequently in the system. The size distributions may also be multimodal, *i.e.*, composed of a series of more or less discrete distributions, with each region having a given modal value. In natural systems, multi-component and multimodal features are frequently observed. The colloidal systems used in this work are all monomodal.

The average particle diameter $\langle d \rangle$ is defined in therms of the frequency, f_i, that is the number of particles of a given diameter d_i:

$$\langle d \rangle = \sum_i f_i d_i. \tag{1.7}$$

In colloidal suspensions, two or more particles can interact via collisions, particle surface effects and hydrodynamic forces. Hydrodynamic interactions arise from a disturbance induced in the fluid flow field by the presence of a particle, which in turn exerts a force on other particles within the range of the flow field. Dispersion forces appear from quantum mechanical effects caused by fluctuations in the electron clouds surrounding atoms. Surface forces result from the proximity of colloidal particle surfaces, which can be electrically charged, it can also absorb ions, nanoparticles, surfactants, polymers, or may be covered with surface-grafted polymers. These forces can act to stabilize or destabilize colloids when the colloidal particles are within the range of the interaction [22].

Colloidal stability relates to the physical state of the system: it is stable if the particles of B remain well dispersed. Unstable colloidal particles will tend to remain together and form aggregates [45]. The hard sphere colloidal particles have Van der Waals attractions which contribute to the formation of aggregates. The attractive forces holding these clusters together are much greater than the typical body forces used in stirring, mixing, milling or ultrasonic mixing. For this reason, colloids are regarded in some cases as being permanently aggregated; this is termed coagulation [21, 45]. Surfactants are frequently used in order to maintain a good dispersion of particles in a colloid.

The properties of a colloid depend on the nature of its components, specially of the dispersed media. In the following section, we will expose the principles of a technique used in this thesis to characterize the linear optical properties of colloids.

1.1.1 Ultraviolet-visible spectroscopy (UV-Vis)

UV-Vis refers to spectroscopy in the ultraviolet (UV) and visible (Vis) spectral regions. This technique gives information about the extinction coefficient of compounds in the linear optical regime. The absorption of ultraviolet or visible radiation by a molecule leads to transitions among its electronic levels. An electronic transition occurs when electrons in an atom are promoted from a lower energy state to an excited state with higher energy. This process requires the absorption of photons whose energy is given by $\epsilon = h\nu$ where h is the Plank constant and ν is the light frequency. UV-Vis spectroscopy is ideal for characterizing the optical and electronic

properties of materials such as: films, powders, solids, and liquids [46].

Absorption in a sample is described by the Lambert-Beer law [6, 46, 47], given by:

$$A_\nu = log_{10}\left(\frac{I_0}{I_T}\right) = l \cdot \varepsilon_\nu \cdot C \qquad (1.8)$$

where A_ν is the absorbance, ε_ν is the extinction coefficient, I_0 is the intensity of the light entering the sample, I_T is the intensity of the light emerging from the sample, l is the pathlength of the sample, and C is the concentration defined as in equation 1.5.

1.2 Nonlinear optical media

Nonlinear optics describes the response of a material when it is irradiated by coherent monochromatic light. Typically, only laser light can provide a beam sufficiently intense to modify the optical properties of a medium [5]. The optical response of materials is described through the relationship between the electric field $\vec{E}$ and the polarization vector $\vec{P}$ [5, 6, 10–12], which is typically described in terms of a Taylor series expansion. The first order term of this expansion represents the linear optics regime, whereas, the higher orders are related to the nonlinear regime.

The relation between $\vec{P}$ and $\vec{E}$ can be obtained from Maxwell's equations. Assuming no external charges $\rho = 0$ and no external currents $\vec{J} = 0$ these are written as: [5, 6, 10–12]:

$$\nabla \cdot \vec{D} = 0; \qquad \nabla \cdot \vec{B} = 0;$$

$$\nabla \times \vec{E} = -\frac{1}{c}\frac{\partial \vec{B}}{\partial t}; \quad \nabla \times \vec{H} = \frac{1}{c}\frac{\partial \vec{D}}{\partial t}. \tag{1.9}$$

Where the displacement vector $\vec{D}$ and the magnetic field vector $\vec{B}$ are given by:

$$\vec{D} = \vec{E} + 4\pi\vec{P}, \quad \vec{B} = \vec{H} + 4\pi\vec{M}; \tag{1.10}$$

$\vec{P}$ and $\vec{M}$ are the electric dipole moment per unit volume, and magnetic moment per unit volume, respectively. We will focus on nonmagnetic media, which means that $\vec{M} = 0$. Using the proper boundary conditions to solve Maxwell's equations (Eqs. 1.9, 1.10), the dipole moment can be expanded in Taylor series of the macroscopic electric field $\vec{E}$. We will consider the second and subsequent terms, which describe the influence of a macroscopic electric field to the dipole moment per unit volume. For some materials, the first term of the Taylor series, P_0, correspond to a dipole within a dielectric, where vanishes [12]. This term only contributes in ferromagnetic materials [12] Under these conditions, the expression of polarization is:

$$P_i = \sum_{j} \chi_{i,j}^{(1)} E_j(\vec{r},t) + \sum_{j,k} \chi_{i,j,k}^{(2)} E_j(\vec{r},t) E_k(\vec{r},t)$$
$$+ \sum_{jkl} \chi_{i,j,k,l}^{(3)} E_j(\vec{r},t) E_k(\vec{r},t) E_l(\vec{r},t) + \cdots, \tag{1.11}$$

If we assume that the polarization depends only on the instantaneous value of the

electric field at time t, which implies that the medium must be lossless and dispersionless, if we also assume an isotropic material, the polarization can be written in a more simple way as [5]:

$$\vec{P}(\vec{r}, t) = \chi^{(1)} \vec{E}(\vec{r}, t) + \chi^{(2)} \vec{E}^{(2)}(\vec{r}, t) + \chi^{(3)} \vec{E}^{(3)}(\vec{r}, t) + ... \qquad (1.12)$$

where $\vec{P}$ and $\vec{E}$ are vectors that have odd parity under inversion symmetry. $\chi^{(m)}$ are the susceptibilities, which are in general tensors. Thus, using the new notation, $\chi^{(1)}$ is a second rank tensor. For isotropic materials, such as gases and liquids, this tensor is diagonal and its elements has the same values. In crystalline media, $\chi^{(1)}$ obeys symmetry properties of the crystal. The susceptibility $\chi^{(2)}$ vanishes in center-symmetrical media as in the case of some crystals, liquids and gases. Third-order nonlinear optical interactions are described by $\chi^{(3)}$ and occur for both, centre symmetric and non-centre symmetric media, in materials of the first kind this tensor vanishes, and in cubic crystals the third order tensor is diagonal [5, 12]. Some phenomena related to the third order susceptibility are four waves mixing and optical Kerr effect. Since optical Kerr effect is a topic of interest of this work, it will be explain in the next section.

1.2.1   Self-focusing and Kerr effect

Kerr Effect

The Kerr effect is a consequence of the changes in the refractive index of materials interacting with an electromagnetic field. In Kerr media, the nonlinear polarization ($\vec{P}$) and the electric field ($\vec{E}$) are related by a third order coefficient as:

$$\tilde{P}(\omega) = 3\chi^{(3)}|\tilde{E}(\omega)|^2\tilde{E}(\omega). \tag{1.13}$$

In Eq.1.11, $\tilde{E}(\omega)$ represents the Fourier transform of the electric field $\vec{E}$. Alterations in the refractive index occur because the electric field affects the electrical susceptibility of the medium in both the real and the imaginary parts ($\chi^3 = Re(\chi^3) + iIm(\chi^3)$). Modifications in the real part lead to changes in the refractive index, while in the imaginary part produce changes in the nonlinear optical absorption [48].

For a linearly polarized electric field $\tilde{E}(\omega)$ interacting with a center symmetrical nonlinear material in which the second order susceptibility is zero, the total polarization is given by:

$$\tilde{P}_{TOT}(\omega) = \chi_{eff}\tilde{E}(\omega), \tag{1.14}$$

where the effective susceptibility is $\chi_{eff} = \chi^{(1)} + 3\chi^{(3)}|\tilde{E}(\omega)|^2$. The refractive index

is related to the effective permitivity as:

$$n^2 = 1 + \chi_{eff} = 1 + \chi^{(1)} + 3\chi^{(3)}|\vec{E}(\omega)|^2 \tag{1.15}$$

On the other hand, an expression for the refractive index is:

$$n = n_0 + 2\bar{n}_2|\tilde{E}(\omega)|^2, \tag{1.16}$$

where n_0 is the linear refractive index and $\bar{n}_2$ is the time average of the second order refractive index, and gives the rate at which the refractive index increases with intensity [5].

Substituting Eq. 1.16 in the left side of Eq.1.15, we obtain:

$$[n_0 + 2\bar{n}_2|\vec{E}(\omega)|^2]^2 = 1 + \chi^{(1)} + 3\chi^{(3)}|\vec{E}(\omega)|^2$$
$$[n_0^2 + 4n_0\bar{n}_2|\vec{E}(\omega)|^2 + 4\bar{n}_2^2|\vec{E}(\omega)|^4] = 1 + \chi^{(1)} + 3\chi^{(3)}|\vec{E}(\omega)|^2 \tag{1.17}$$

Correcting up to second order terms in equation 1.17, we can relate the linear and nonlinear refractive indices with the corresponding linear and nonlinear susceptibilities by the following expressions:

$$n_0 = (1 + \chi^{(1)})^{1/2}, \tag{1.18}$$

$$\bar{n}_2 = \frac{3\chi^{(3)}}{4n_0}. \tag{1.19}$$

It is useful to express the refractive index as a function of the luminous intensity I:

$$n(I) = n_0 + n_2 I, \tag{1.20}$$

this equation describes the optical Kerr effect [6], where n_2 is the second order refractive index and the luminous intensity I is defined as:

$$I = 2\epsilon_0 n_0 c |\vec{E}(\omega)|^2. \tag{1.21}$$

Substituting I in Eq.1.20 and comparing with Eq. 1.16, the relationship between n_2 and $\bar{n}_2$ can be expressed as [5]:

$$n_2 = \frac{\bar{n}_2}{\epsilon_0 n_0 c}, \tag{1.22}$$

and n_2 is related with the susceptibility by:

$$n_2 = \frac{3\chi^{(3)}}{4n_0^2 \epsilon_0 c}. \tag{1.23}$$

Kerr materials obey above equations and induce other effects as self-focusing, which

is explained in the next section.

Self-focusing effect

In general, a self-induced nonlinear optical effect is a consequence of the interaction of the optical beam with a given medium during propagation [5, 14, 15]. Consider a laser beam with a Gaussian transverse profile propagating in a medium with refractive index given by Eq. 1.20. Changes in n_2 are induced. If the change in n_2 is positive, the central part of the beam having a higher intensity should experience a larger refractive index than the edge; therefore, it will travel at a slower velocity than the edge. Consequently, as the beam traverses the medium, the original plane wave-front gets progressively more distorted [11], as depicted in Fig. 1.2. This is know as the self-focusing effect and can occur when a high intensity beam interacts with Kerr media.
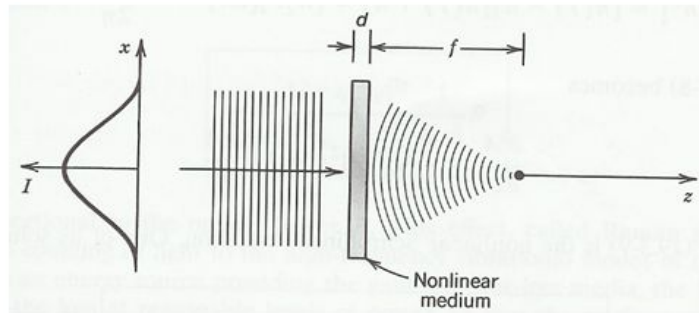
Figure 1.2: Depiction of a plane wave with Gaussian profile interacting with a Kerr media inducing the self-focusing effect [6].

A beam traversing a Kerr medium will experience self-focusing when the optical power reaches a critical value $P_{cr} = \frac{\varrho \lambda^2}{4\pi n_0 n_2}$, where $\varrho = (\frac{1.22\pi^2}{8} \approx 1.8362)$ [5, 49]. The

opposite effect, *i.e.* self-defocusing, occurs if the response of the medium is negative (changes in n_2), leading to and increase of the natural diffraction.

1.2.2   Characterization of nonlinear media: Z-scan technique

The Z-scan technique is one of the most widely used methods for the characterization of nonlinear optical media because of its accuracy and simplicity [50]. It is a single-beam technique that measures both, the nonlinear refractive index and the nonlinear absorption coefficient, for a wide variety of materials [50–52].

The conventional experimental setup is depicted in Fig. 2.2. A continuous wave (CW) laser is focused by a lens. In front of the lens, the sample is mounted on a single axis translational stage oriented along the propagation axis (optical axis), designated as the z-direction. An aperture is placed in front of a photodetector located at the far field distance (120 Z_R [1] or more) from the lens.
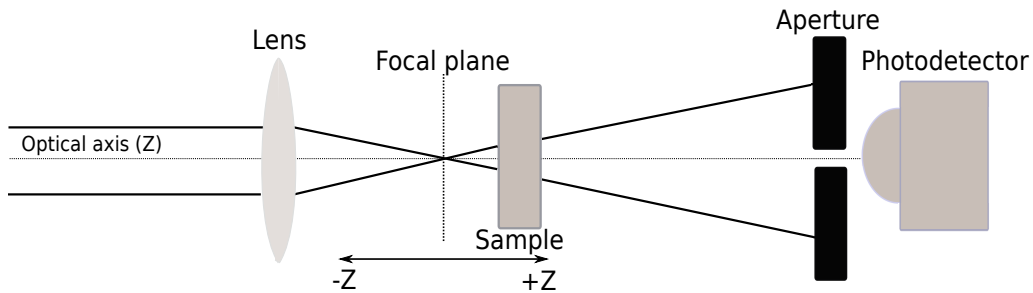
Figure 1.3: Typical Z-scan setup: the sample is placed behind the focusing lens. The sample is moved along the optical axis around the focal plane. The photodetector is placed behind an aperture to capture the transmitted light.

---

[1]Z_R is the Rayleigh distance, $Z_R = \frac{2\pi\omega_0}{\lambda}$, where ω_0 is the beam waist.

By displacing the sample with the translational stage, the far-field intensity is measured in the photodetector as a function of the position of the sample along the propagation axis (z), with $z = 0$ being the beam waist of the focused Gaussian beam.

The samples are characterized using two detection schemes: one called the closed-aperture scheme, used to determine the nonlinear refraction, and the other called open-aperture scheme, which yields the nonlinear absorption. Data for both, the nonlinear refraction and nonlinear absorption, are then provided by the optical transmittance curves obtained with the photodetector as a function of the position of the sample with respect to the focal point.

For the close-aperture scheme, the sample can be located in three regions respect to the focal point. When the sample is located before the focal plane ($z < 0$) (Fig. 1.4a), and if it exhibits a positive nonlinear optical response ($\Delta n_2 > 0$), the natural waist of the beam is shifted towards the sample due to the self-focusing effect, causing the beam to expand further in the far field. Then, the light collected by the detector decreases (1.4a). Just after the focal plane ($z \approx 0$), the intensity captured by the detector is maximum and the transmittance curve shows a peak (1.4 b). Finally, for larger $z > 0$ (1.4c)), the transmittance returns to its original level [53].

In the closed-aperture scheme, the transmittance curve exhibits a minimum (valley) first, followed by a maximum (peak) (*i.e*, a valley-peak transition denoted as T_{v-p}), indicating that the sample has a positive nonlinear refractive index (also shown
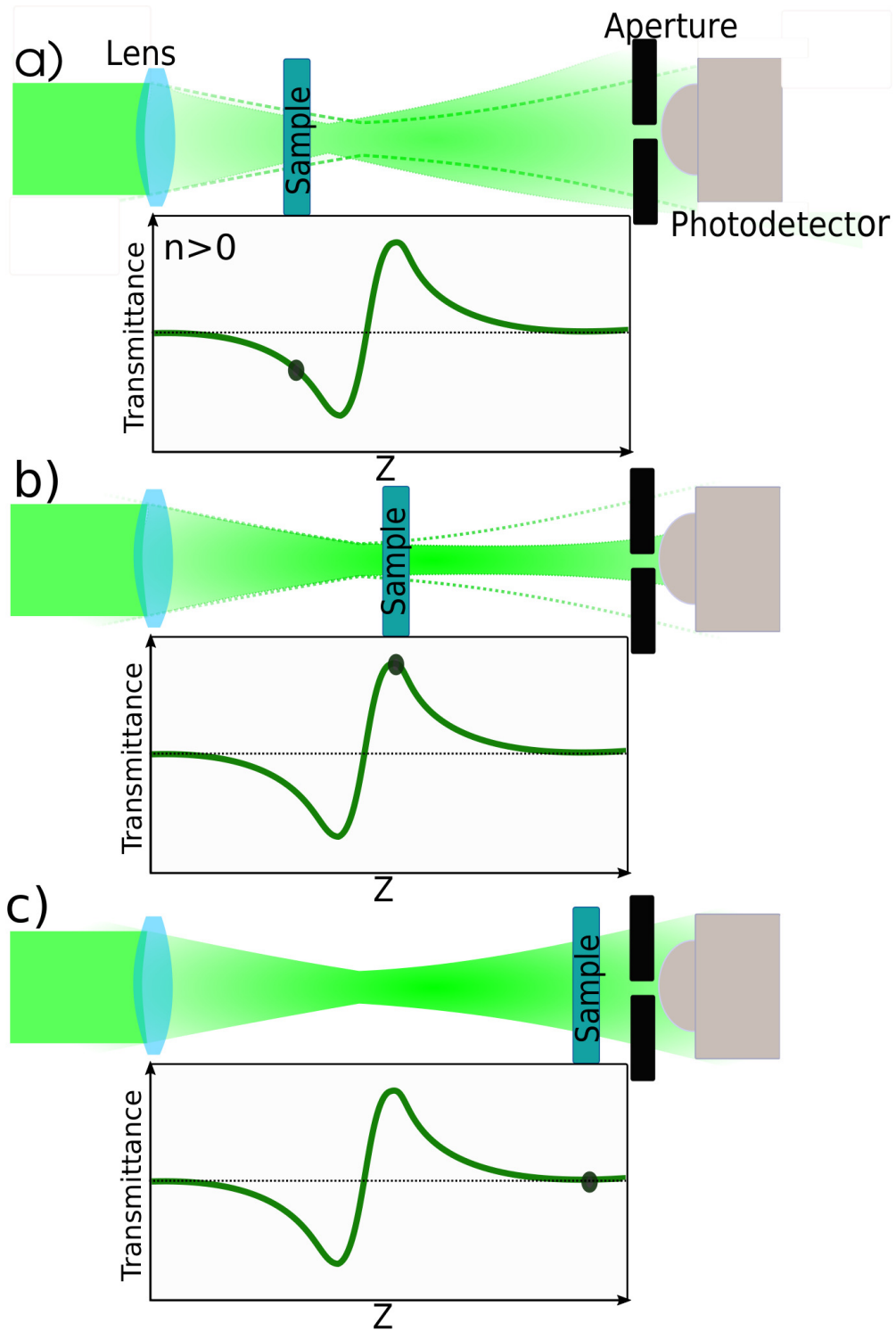
Figure 1.4: The Z-scan measurement. The change of the laser beam and the corresponding change of the transmittance is shown for three different sample positions: *a)* before the focal plane, *b)* just after the focal plane, and *c)* far away from the focal plane.

in Fig.1.4). The opposite situation (*i.e*, a peak-valley transition T_{p-v}) indicates a negative nonlinearity $\Delta n_2 < 0$. Typical z-scan curves showing the refraction response of two nonlinear media are shown in figure 1.5. Regarding the open-aperture scheme, a valley indicates positive nonlinear absorption, whereas a peak indicates a self-transparency effect or negative nonlinear absorption.
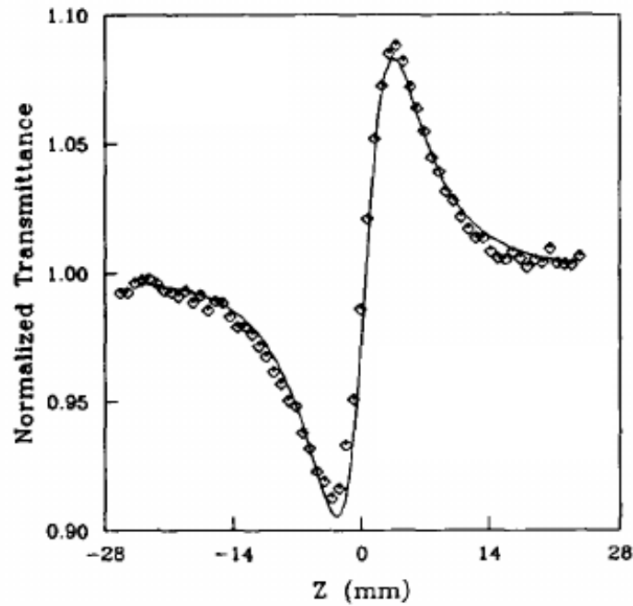
Figure 1.5: Typical Z-scan curve with a positive nonlinearity (valley-peak). The solid line is a calculated curve and dots are experimental data, the sample was a CS_2 cell [51].

In general, nonlinearities of any order can be considered in the Z-scan analysis. The simplest model [51] assumes a Gaussian beam with waist w_0 and Rayleigh distance z_R traveling in the $z > 0$ direction, which passes through a thin sample of a medium with a cubic nonlinear response (thickness of the order of z_R). In this model, the nonlinear absorption is neglected. The transmittance difference between peak and valley (ΔT_{p-v}) is related to the change in the refractive index Δn_2. The distance

between the peak and the valley Δz_{p-v} of the Z-scan curve gives information about a property of the medium called locality. A material is said to be local if its nonlinear optical response is restricted to the size of the incident beam. If $\Delta z \cong 1.7 z_R$ the medium can be considered to be local [51].

In nonlocal materials, the change in refractive index due to nonlinear effects extends well beyond the beam profile. It can be demonstrated that the separation between the peak and the valley of of the Z-scan curves (Δz) for nonlocal materials can be extended for a region which is bigger than the size of the incident beam. Changes of ΔT_{p-v} and Δz_{p-v} depend on both, the nonlocality of the material and the magnitude of phase changes $\Delta \Phi_0$ [51].

On the other hand, in the open-aperture scheme, the Z-scan technique becomes insensitive to nonlinear refraction and results in a null signal *i.e.* flat response with Z, unless nonlinear absorption is present [52]. In this case, a symmetrical curve showing a reduced transmittance (valley) about the focal point position correspond to the negative nonlinear absorption. The opposite situation (peak) indicates a self-transparency effect or positive nonlinear absorption. A typical curve of negative nonlinear absorption is shown in Fig. 1.6. It is important to point out that in the open-aperture scheme, the purpose is to collect as much as possible of the transmitted light with the photodetector. For this reason, the experimental configuration can be modified in such way [54, 55]

In order to account for other properties of the samples, a variety of theoretical models have been proposed. For example, in absorbing media, heating produced by the
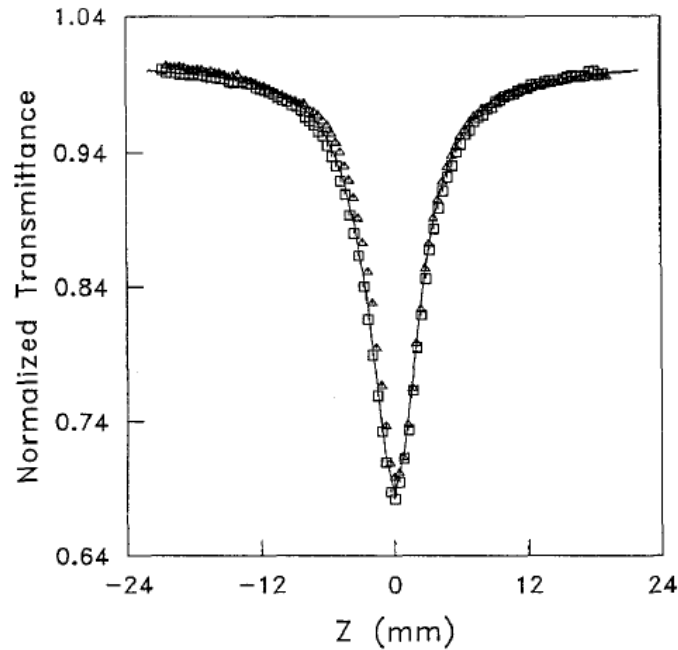
Figure 1.6: Typical open-aperture Z-scan curve. In this case the valley indicates negative nonlinear absorption [52].

incident light induces a change in temperature. As a consequence, the density and the refractive index of the sample change accordingly. These thermal effects have been considered in the so-called thermal lens model [56–58]. Similarly, other models have accounted for the thickness of the sample [59], leading to more elaborated and realistic descriptions of nonlinear media. As we will show in Chapter 2, samples characterized by Z-scan technique are thick. They present nonlinear absorption and evidence of nonlocal behavior. So far, the existing models consider only thin samples and nonlocality or nonlinear absorption separately. However, even when there are no available models to provide a quantitative description of our experimental system, the Z-scan technique is still useful to provide a qualitative description of the nonlinear response.

1.2.3   Optical Spatial Solitons (OSS)

Solitary waves arise as consequence of compensation of linear and nonlinear effects leading to a wave that remains unchanged on propagation, they can be either temporal or spatial [7, 14]. Temporal solitons are optical pulses that maintain their shape over time during propagation [14]; these can be observed in non dispersive media such as silica glass fibers [7]. Spatial solitons are self-trapped beams of finite spatial cross section [48, 60]. These beams travel without the divergence associated with diffraction, they remain confined in the transverse directions orthogonal to the direction of propagation.

Both types of solitons appear as the consequence of change in the refractive index of an optical material produced by optical Kerr effect. In Kerr media, changes of the refractive index lead to spatial self-focusing (or self-defocusing) and temporal self-phase modulation (SPM). These two effects are responsible for the formation of optical solitons. A spatial soliton is formed when the self-focusing of an optical beam balances its natural diffraction forming an OSS [14].

To understand the mechanism for OSS formation through the self-focusing effect, we can think of a beam propagating through a homogeneous medium. In this situation, the beam tends to diffract spreading its profile with a positive curvature as shown in (Fig. 1.7 a). The diffraction (Fig. 1.7 b) can be compensated if the refractive index increases as observed with the self-focusing effect. Under this situation the beam can become self-trapped along the trajectory of the propagation direction (Fig. 1.7 c).
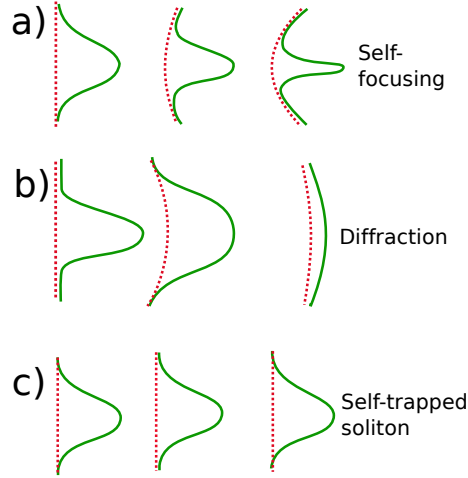
Figure 1.7: A) Self-focusing. B) Diffraction y C) Soliton propagation. Red dashed lines represents the wave-front, while solid lines the beam profile [14, 60].

OSS propagation can be mathematically described upon considering the slowly varying envelope approximation for the electric field expressed as:

$$\vec{E}(\vec{r}, t) = A(r)exp(i\beta_0 z), \tag{1.24}$$

The equation governing the evolution of optical fields in nonlinear medium has the same form as the nonlinear Schrödinger equation (NLS). In a nonlinear Kerr medium, the light propagation can be described by [14]:

$$2i\beta_0 \frac{\partial A}{\partial z} + \nabla_\perp^2 A + 2\beta_0 k_0 n_{NL}(I)A = 0, \tag{1.25}$$

where $\beta_0 = k_0 n_0 \equiv 2\pi/\lambda$, and $\lambda = 2\pi c/\omega_0$ is the wavelength . Eq. 1.25 I is the field intensity ($I = (\frac{n_0 \epsilon_0}{2})|\vec{E}|^2$).

When nonlinear and diffraction effects are included, the envelope A varies with z on a scale much longer than the wavelength λ (paraxial approximation), the second derivative d^2A/dz^2 can be neglected [14]. In the absence of nonlinear effects, this reduces to the well-known paraxial equation. We focus on the case of the third order nonlinearity and use n_2, which is the Kerr coefficient. To simplify the form of the Eq 1.25, it is useful to introduce scaled dimensionless variables as:

$$x = X/w_0, \quad y = Y/w_0, \quad z = Z/L_d, \quad u = (k_0|n_{NL}|L_d)^{1/2}A, \tag{1.26}$$

where w_0 is a transverse scaling parameter related to the input beam width and $L_d = \beta_0 w_0^2$ is the diffraction length. In terms of these dimensionless variables, Eq. 1.25 takes the form of a standard $(2+1)D$ NLS equation

$$i\frac{\partial u}{\partial z} + \frac{1}{2}\nabla_\perp^2 u \pm |u^2|u = 0. \tag{1.27}$$

The choice of the sign for the third term of this expression depends on the sign of the nonlinear parameter n_2. The first term describes the propagation of the beam; its transverse evolution is described by the laplacian while the last term contains the characteristics of the material, which are intensity dependent.

The solutions of Eq. 1.27 are only feasible in 1D, in this case, self-focusing media allows for the stable $(1+1)D$ spatial solitons [6, 7, 11, 14, 15]; and the equation is

rewritten as:

$$i\frac{\partial u}{\partial z} + \frac{1}{2}\frac{\partial^2 u}{\partial x^2} + |u|^2 u = 0, \tag{1.28}$$

To solve Eq 1.28 we can propose a function with the form:

$$u(z,x) = V(x)exp[i\Phi(z,x)], \tag{1.29}$$

where V is independent of z, and maintains its shape during propagation, Φ is the phase which can depend on both z and x. After substitute Eq. 1.29 in Eq. 1.28 it can be obtained the fundamental mode of the solution, this is known as fundamental soliton and corresponds to a bright spatial soliton [14].

$$u(z,x) = a\,\mathrm{sech}(ax)exp(\frac{ia^2 z}{2}), \tag{1.30}$$

where a is the soliton amplitude and come from the boundary conditions which give $\phi = \frac{a^2 z}{2}$.

Two-dimensional NLS can be solved numerically only, the solutions describe the $(2+1)D$ optical solitons in Kerr media, but they are unstable due to the critical collapse at high optical powers [61].

The OSS appear as consequence of the nonlinear response of colloidal suspensions, which is related to the optical forces exerted by light on the particles. In particular the optical gradient force, which will be explained in the next section.

1.2.4   Optical forces in colloids

The influence of an electric field on dielectric particles has been widely studied for its applications in optical tweezers [62, 63]. Consider a transparent, homogeneous, isotropic, non-magnetic spherical particle with radius a and refractive index n_p, suspended in a medium with smaller refractive index n_m. If the radius of the particle is larger than the wavelength of light (λ), the approximation of ray optics describes the interaction adequately [4]. On the other hand, when $a \ll \lambda$, the description corresponds to the so called Rayleigh regime. Although the initial electrostatic charge distribution is random, an external electric field induces a net electric dipole withing the material. The magnitude of the polarization $\vec{P}$ per unit of volume is:

$$\vec{P} = \frac{N}{V}\vec{p}, \tag{1.31}$$

where N is the number of atoms or molecules in a volume V of material and $\vec{p}$ is the polarization of an isolated molecule [62]. Therefore, this particle acts as an electric dipole with dipole moment $\vec{p}_{sp}$, parallel to the applied electric field, which can be expressed as [62]:

$$\vec{p}_{sp} = \alpha\vec{E} \tag{1.32}$$

We can thus define the polarizability $\alpha = p_{sp}/E$ of the small sphere. It is common to write α in terms of the refractive index of both, the particle (n_p) an the suspending

media (n_b) as:

$$\alpha = 3V n_b^2 \epsilon_0 \frac{m^2 - 1}{m^2 + 2}, \tag{1.33}$$

$V = 4/3\pi a^3$ is the volume of the sphere, $m = \frac{n_p}{n_b}$. Eq. 1.33 is known as the Clausius Mossotti relation [62].

Consider two particles of mass m carrying charges $\pm q$, located at $\vec{r}_{\pm}$, and separated by a distance $\Delta \vec{r} = \vec{r}_+ - \vec{r}_-$, so that they form a dipole of magnitude $p_d = q\Delta r$.the total force F can be expressed as:

$$\vec{F} = \frac{1}{4}\alpha \nabla |\vec{E}|^2 + \frac{\sigma_{ext,d}}{c}\langle \vec{S} \rangle - \frac{1}{2}\sigma_{ext,d}c\nabla \times \vec{s}_d, \tag{1.34}$$

In Eq. 1.34, $\langle \vec{S} \rangle$ is the time-averaged Poynting vector which is defined as: $\vec{S} = \frac{1}{2}Re(\vec{E} \times \vec{H}^*)$ (the symbol $*$ denotes the conjugate of H). In the last term of Eq. 1.34, the time-averaged spin density of the incoming wave, has the following form: $s = i\frac{\varepsilon_0}{2\omega}\vec{E} \times \vec{E}^*$ [62]. The net force involves both, the gradient and scattering forces $\vec{F} = \vec{F}_{grad} + \vec{F}_{scat}$ [62,64]. The first term in Eq. 1.34 is the gradient force which can be rewritten in terms of the intensity I, as:

$$\vec{F}_{grad}(\vec{r}) = \frac{1}{2}\alpha n_b \nabla I(\vec{r}); \tag{1.35}$$

where α is given by the Eq. 1.33.

The gradient force is responsible for particle confinement in optical tweezers. This is a conservative force because it arises from the potential energy of a dipole in the electric field. Therefore, particles with positive polarizability ($\alpha > 0$), *i.e.*, particles whose refractive index is higher than that of the surrounding medium, are attracted towards the high-intensity region of the optical field, and particles with negative polarizability ($\alpha < 0$), are repelled by the high-intensity regions.

The second term in Eq. 1.34 is the scattering force, which temporal average value can be written as:

$$\vec{F}_{scat}(\vec{r}) = \frac{\sigma_{ext}}{c} \langle \vec{S}(\vec{r}) \rangle. \tag{1.36}$$

In terms of the intensity, the scatering force can be expressed as:

$$\vec{F}_{scat} = \frac{I}{c} \frac{128\pi^5 a^6}{3\lambda^4} n_b \left(\frac{m^2 - 1}{m^2 + 2}\right)^2 \hat{S}(\vec{r}) \tag{1.37}$$

This force is non-conservative and is due to the transfer of momentum from the field to the particle as a result of the scattering and absorption processes. Notice that $\vec{F}_{scat}$ is proportional to the extinction cross-section of a spherical particle, $\sigma_{ext} = \frac{128\pi^5 a^6}{3\lambda^4} \left(\frac{m^2-1}{m^2+2}\right)^2$ and points in the direction of the Poynting vector.

For Rayleigh particles, using a Gaussian beam of focal spot size ω_0 in the axial position $z = \frac{\pi\omega_0^2}{\sqrt{3}\lambda}$, the ratio between F_{grad} and F_{scat} can be written as [64]:

$$R = \frac{F_{grad}}{F_{scat}} = \frac{3\sqrt{3}}{64\pi^5} \frac{n_b^2}{\left(\frac{m^2-1}{m^2+2}\right)} \frac{\lambda^2}{a^3\omega_0^2} \tag{1.38}$$

Eq. 1.38 provides an estimate of the predominant force depending on the particle diameter and the refractive index.

Dielectric nanocolloidal suspensions are an effective Kerr-like medium. In that suspension, the nonlinear response attributed to optical gradient force (Eq. 1.35), which depends of the light intensity, this force works against or in favor of diffusion, depending on α sign, and concentrate (repels) the particles within the high (low) intensity region of a Gaussian beam [16]. To describe this situation, we can consider an optical beam within a colloid, in this situation the particle velocity distribution is locally Maxwellian [65] and the particle current density is equal to:

$$\frac{\partial \rho}{\partial t} + \nabla \vec{J} = 0, \tag{1.39}$$

where $\rho(\vec{r}, t)$ is the particles density and $\vec{J}(\vec{r}, t)$ the current particles density [65] which is equal to:

$$\vec{J} = \mu\rho(\vec{F}_{ext} + \vec{F}_{int}). \tag{1.40}$$

Where $\vec{F}_{ext}$ is the gradient force and $\vec{F}_{int}$ is the net force acting on the colloidal particle. The equation 1.40 can be rewritten as:

$$\vec{J} = \mu\rho\vec{F}_{ext} - D\nabla(\rho(Z(p))), \tag{1.41}$$

where μ is the particle mobility, $D = \frac{\mu}{\beta}$ is the difussion constant, $\beta = \frac{1}{k_B T}$ and $Z(\rho)$ is a terms which contains the particles interaction. In a model given by Matuszewski and coworkers [65] the particle interactions is describe by a hard sphere potential. The current particles induces a nonlinear refractive index change, in these conditions we assume a stationary state, $(\partial\rho/\partial t) = 0$ and equilibrium conditions $\vec{J} = 0$. The nonlinear propagation of a beam in a nanocolloidal suspension can be described by an equation similar to NLS which can be written in the following form:

$$i\frac{\partial\Psi}{\partial z} + \frac{1}{2k_0 n_m}\nabla^2\Psi + F(\rho)\Psi = 0 \tag{1.42}$$

where the optical field is given by $\vec{E}(\vec{r}, t) = \Psi(\vec{r})exp[ik_0 n_m z - \omega t]$, ω its frequency, and n_m is the refractive index of medium in absence of light. $F(p)$ represents a complex function of the particle density (or concentration) whose real and imaginary parts are associated with the refractive index and Rayleigh scattering loss, respectively [8]. The nonlinearity is also incorporated in this term that may also include other parameters such as the particle density $\rho(r)$, which in turn depends on the intensity distribution of the incident light beam.

Nonlinear optical properties and OSS formation in dielectric nanocolloids

In this chapter, we report an experimental study of the nonlinear optical properties of dielectric nanocolloids with positive polarizability ($\alpha > 0$). The Z-scan technique is used to evaluate the nonlinear refractive indices of the nanocolloids used for the experiments. Given their nonlinear properties, we evaluate the performance of this kind of media for the generation of optical spatial solitons (OSS) in two transverse dimensions. A detailed experimental study on the formation of these self-trapped beams in dielectric colloidal media is presented. OSS formation and propagation are evaluated as a function of different parameters of the colloid such as particle size and concentration.

2.1 Sample preparation and characterization

The colloidal suspensions used in this work were formed by polystyrene nano-spheres ($n_p = 1.60$) suspended in distilled water ($n_b = 1.33$). Four suspensions were made following the results from previous works using these kinds of colloids [1, 8]: two particle diameters were chosen, and for each of them solutions with two different concentrations were made. The mean value diameter of the particles were $62\ nm$ and $77\ nm$, and the concentrations were $C = 0.5\%$-solids and $C = 1\%$-solids of the total volume. The sizes and initial concentration of the particles were taken as provided by the manufacturer (*Bangs Laboratories* [66]). The number of products were Cat $\#\ L031030C$ and Cat $\#\ L0970716C$ respectively. To obtain the concentrations used for the experiments, the original solutions were diluted in distilled water. To dilute the colloids, we use the relation $C_iV_i = C_fV_f$, where the initial concentration is $C_i = 10\%$-solids of the total volume, V_f and C_f are the aimed volume and concentration, and the initial volume is the variable to be determined; to obtain. For example, $C_f = 0.01$ (1%-solids), $C_i = 0.1$ and $V_f = 0.5\ ml$, therefore, $V_i = \frac{C_fV_f}{C_i}$.

2.1.1 UV-Vis spectroscopy

The four nanocolloidal suspensions were analyzed by UV-Vis spectroscopy (Thermo spectrometer, Evolution 600). The extinction curves obtained for all samples are shown in Fig. 2.1. For all the samples, the curves decay as the wavelength increases. Notice however that in all cases, the linear absorption does not reach a zero value for the wavelength of the laser used for the experiments (532). Therefore, the extinction

of these nanocolloids may be attributed to the light scattering and the polystyrene linear absorption coefficient, which is 5 cm^{-1} [67]. As discussed in the final section of this chapter, this is relevant for thermal effects induced in the sample that may hamper the formation of OSS.
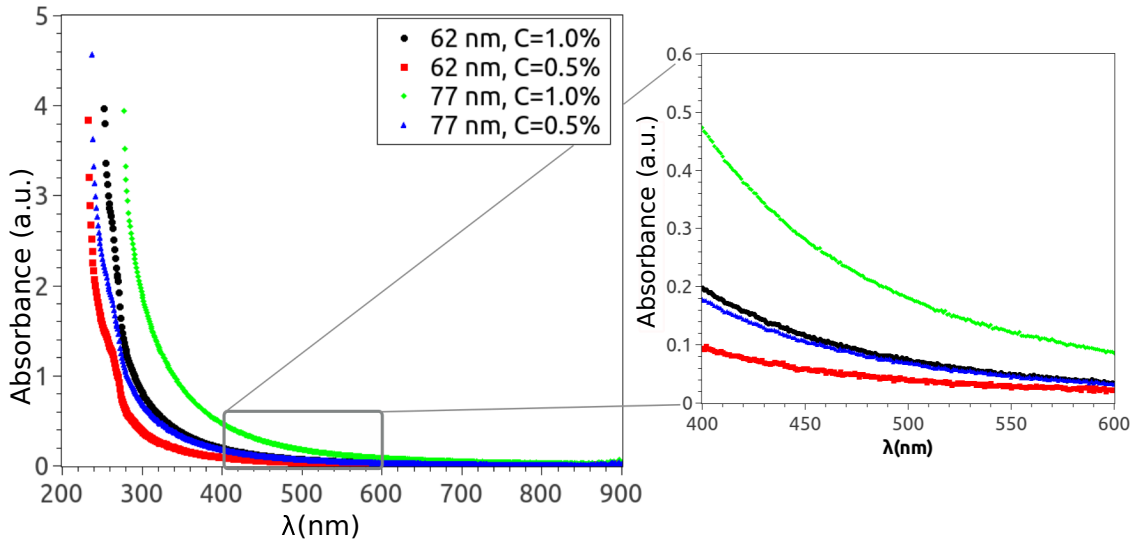
Figure 2.1: UV-Vis curves obtained for the nanocolloidal samples used for the experiments. The left curves shows the absorbance for the full spectral range covered by the spectrometer; the curve on the right shows more details (zoom in) of the spectral region centered at $\lambda = 532\ nm$.

2.1.2 Z-scan technique

The nonlinear optical response of the dielectric nanocolloids was evaluated via Z-scan technique, using the set-up depicted in Fig. 2.2. A continuous wavelength (CW) laser beam (Coherent Verdi V5, 532 nm), with a Gaussian beam profile and optical powers ranging from 0.8 W to 1.4 W is focused onto the samples by a

convergent lens with a focal length of 2.54 *cm*, yielding a calculated beam waist [1] of 7.5 *µm*. The liquid sample is contained in a 1 *mm*-width quartz cuvette attached to a computer-controlled motorized translation stage, allowing for an accurate and controlled motion along the z-axis using steps of 7 *µm* ±0.05 *µm*. For the closed-aperture scheme, the photodetector [2] is located 90 *cm* away from the focusing lens and a diaphragm with an aperture of 1.2 *mm*-diameter is placed in front of the photodetector. In open-aperture measurements, the photodetector [3] is placed in touch of the output glass wall of the sample container on the same holder as the cuvette, capturing the light transmitted through the sample (this scheme is not shown in Fig.2.2).
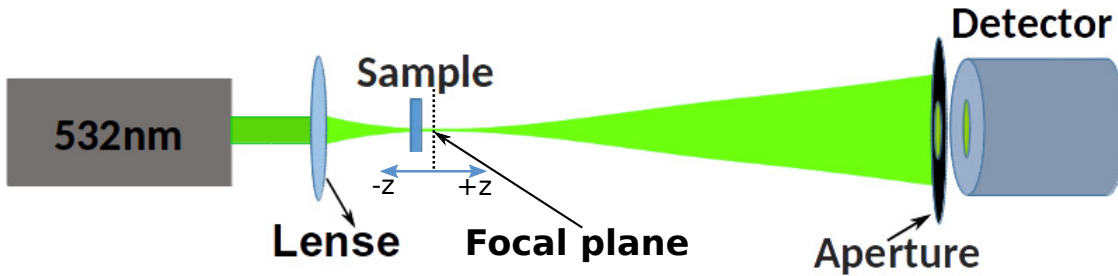
Figure 2.2: Z-scan arrange.

The transmittance curves obtained with Z-scan technique were normalized using the mean value of the first and the last transmittance intensity measurements. The curves were registered using a fixed laser power of 1 *W*. For the closed-aperture scheme (Fig. 2.3(*a*)), the curves are asymmetric, with a valley-peak transition (*i.e.*,

---

[1]To calculate the beam waist we used the conventional Gaussian beam equations shown in reference [6], pag. 87.

[2]Photodiode Thorlabs S151C, with a resolution of 100 *pW*, response time of 1 *µs* and a power range of 1nW-50mW.

[3]The photodetector was thermal power sensor a Thorlabs S302C, with a resolution of 1 *mW*, response time of 1 *s* and power range of 100 *µW*-2 *W*.

a minimum followed by a maximum) indicating that the samples exhibit a positive nonlinear response (*i.e.*, a positive nonlinear refractive index). For the colloid with $62\,nm$-particles, the highest concentration ($C = 1.0\%$) exhibits the largest nonlinear response $\Delta T_{v-p} = 2.25$, whereas the lowest response ($\Delta T_{v-p} = 1.75$) is observed for the colloids with $77\,nm$-particles with $C = 1.0\%$. This shows that the optical nonlinear response indeed depends on the particle diameter d and concentration C.
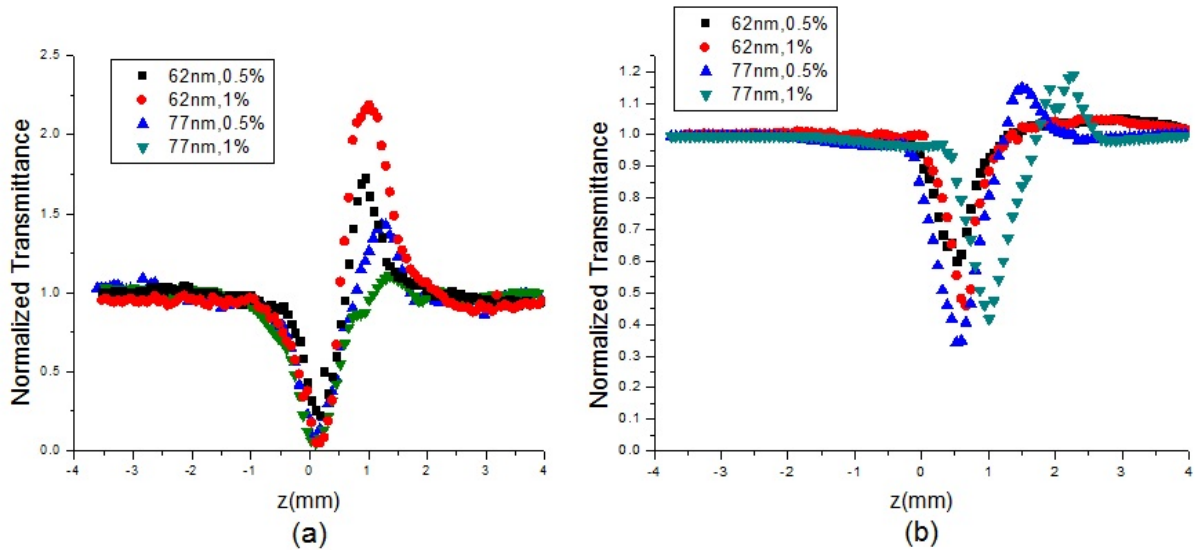
Figure 2.3: z-scan curves for an incident power of $1\,W$. (a) Closed-aperture detection showing the nonlinear refractive index. (b) Open-aperture detection showing the nonlinear absorption.

These Z-scan curves do not exhibit the typical features obtained for Kerr-type local media; the values for Δz_{v-p} ($\Delta z_{v-p} = 0.95\,mm = 2.45\,z_R$) are larger than the typical value of ideal Kerr local media ($\Delta z = 1.7 z_R$). In fact, values of Δz_{v-p} similar to the ones obtained here have been achieved when the nonlinear optical response has a nonlocal character [68, 69].

In the case of the open-aperture scheme, Fig. 2.3(b), several aspects can be pointed

out from the normalized transmittance curves. For the 62 *nm*-diameter particles, there is a nonlinear positive absorption, with a larger magnitude for the highest concentration. The nonlinear absorption can be attributed mainly to scattering losses. In contrast with the linear extinction (Fig. 2.1), occuring when the particles are homogeneously distributed, in this case scattering is enhanced around the highest intensity regions due to the accumulation of particles.

The samples with 77 *nm*-diameter particles, on the other hand, exhibit a different behavior; a valley-peak transition is observed. The valley indicates a positive nonlinear absorption and the peak a self-transparency effect [54]. Notice as well that there is a shift of the curves away from the focal plane, which is larger for the largest concentration. We believe that both these characteristics might be due to thermal effects, attributed to the higher linear extinction of these samples (Fig. 2.1). If the sample is locally heated by the intense laser light, there might arise a thermophoretic effect [70], opposite to the optical gradient force, which would cause a depletion of particles at the central part of the beam. As we are using a CW laser, the heating would be cumulative, implying a delay in the thermal response which would explain the shift of the curves and the peak after the valley.

Although the Z-scan curves cannot provide quantitative information because there are no available theoretical models that consider simultaneously a thick sample, nonlinear absorption and nonlocality, the curves do provide important qualitative information. In particular, we could verify that all the samples present a positive nonlinear response. Moreover, the importance of the particle size and concentration becomes evident from the different characteristics observed in the Z-scan curves for

both refraction and absorption.

2.2   Formation and characterization of optical spatial solitons

To investigate the generation of optical spatial solitons OSS, the same samples used for Z-scan experiments were analyzed. The goal was to identify the experimental parameters allowing for the formation of OSS. From the Z-scan results, it was evident that the particles size and concentration play a role in the nonlinear optical response of the nanocolloids. Therefore, certain differences in OSS formation are to be expected for different particle sizes (62 nm and 77 nm) and concentrations ($C = 0.5\%$ and 1.0%).

The experiments for OSS formation were performed using the setup illustrated in Fig. 2.4. The laser beam (same features as described for the Z-scan experiments) with an initial diameter of 2.25 mm, was focused with a microscope objective $MO1$ onto a glass sample cell (dimensions 6 $mm \times$ 6 $mm \times$ 2 mm). The cell container was filled and sealed once the nanocolloidal sample was introduced. We used the scattered light from the particles to observe the beam propagation within the sample; this was recorded from the top of the cell with a camera. Simultaneously, the cross section of the beam was recorded by a second camera placed at the output of the cell. This CCD camera is part of a front-view system which also includes a second microscope objective $MO2$, a filter to avoid image saturation, and an eyepiece lens

L, as shown in Fig2.4.
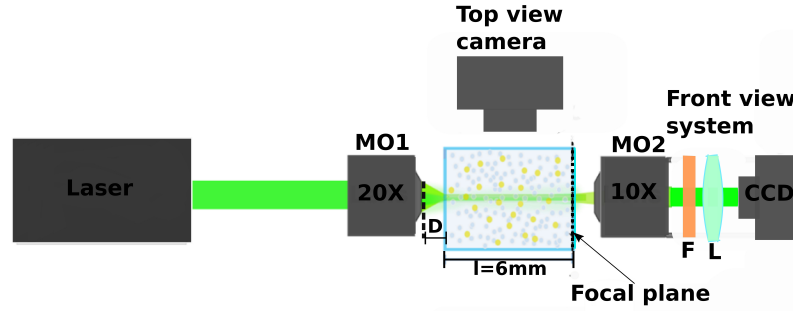
Figure 2.4: Experimental setup to investigate the generation of solitons: microscope objectives (MO), lens (L), filter (F).

Using a fixed input power, videos were recorded with the front-view system to measure the width of the cross section of the beam. In each video frame a Matlab algorithm (described in Appendix A) was used to obtain an intensity beam profile which was fitted to a Gaussian curve. Using the fitting parameters, the width values obtained from different frames in the same video were further averaged to obtain the final beam width for a fixed incident power. This process is illustrated in Fig. 2.5.

Two parameters were analyzed for OSS formation: the input power (P) and the distance D between the objective $MO1$ and the input face of the sample cell. For a given value of D, the size of the spot reaching the sample is fixed, in these circumstances the maximum intensity only depends on the input power P. In this case, the nonlinear optical regime in colloids is attained at certain power level $P \cong 1W$ [1]. As for the distance D, this parameter is related to the position of the focal plane of the input beam. It affects the actual size of the beam entering the sample, and therefore the intensity, as well as the curvature of its wavefronts. Accordingly, the
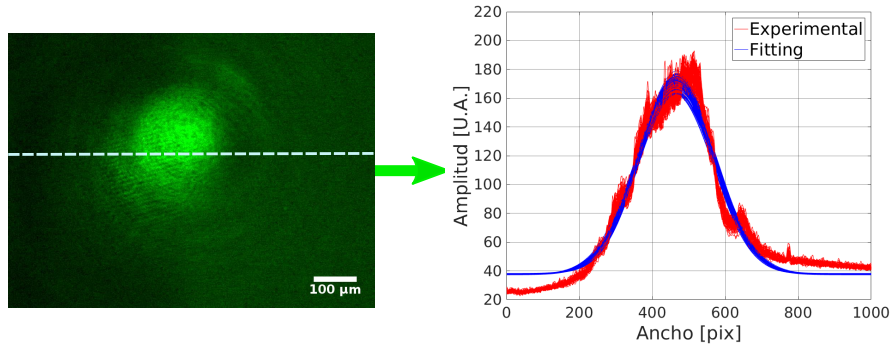
Figure 2.5: The picture on the left shows the cross section of the beam at the end of cell container, the dash line indicates the region where the beam profile is obtained. On the right the beam profile (red curve) and the Gaussian fitting curves (blue) are shown.

two parameters, P and D, determine the maximum optical intensity reached within the sample.
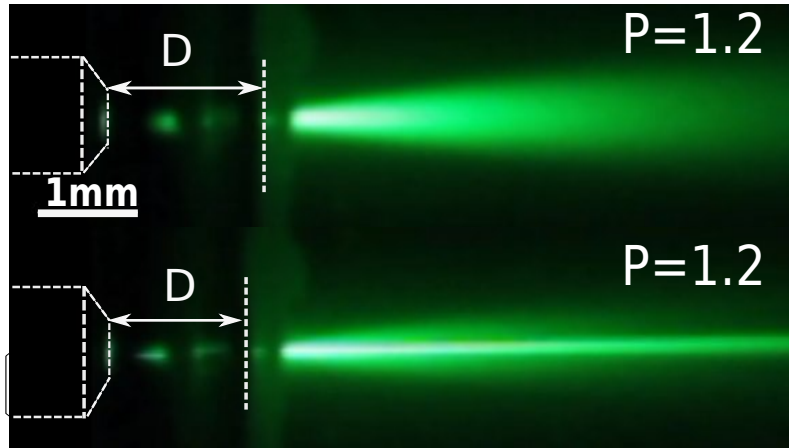
Figure 2.6: Top view camera images, the top picture shows the cell position far away from the objective, the bottom picture shows the cell in D_c position.

The influence of the distance D (see Fig. 2.6) on OSS formation was evaluated following a systematic procedure. First, the glass cell container was placed in contact with the microscope objective $M01$; subsequently, the cell was displaced away from

$MO1$ along the beam path using the kinematic stage. Videos were recorded during this process using the front-view system. Hence, measurements of the transverse size of the beam for different cell positions were made starting with the cell in contact with $M01$. When the OSS is formed, the cross section of the beam is minimum, and if the stage is still moving in the same direction, the beam width will start to increase again. Specifically, we observed that there is a critical value of the distance $D = D_c$, after which it is not possible to obtain an OSS anymore, regardless of the optical power.

The widths of the beam registered with the procedure described above are presented in Fig. 2.7. As shown in the figure, the width (diameter) of the beam measured at the output of the sample cell varies with D. Although the widths obtained for the samples with 62 nm-particles do not show a clear trend (Fig.2.7(a)), there is an interval of D for which the output beam is smaller. The samples with particles of $77nm$ have a different behavior depending on the concentration. At 1%, there is clearly an optimal position of the sample to obtain the narrowest output beam (Fig. 2.7(b)). For the concentration of 0.5%, the width of the output beam is approximately constant for $D < 0.6mm \approx D_c$, and it drastically increases for $D > D_c$. We noticed that the optimum and/or critical value of D varies depending on particle size and concentration. The plots of Fig. 2.7 were obtained for an incident power of $P = 0.6\ W$, which is close to the threshold to start observing self-focusing (see below).

Once the optimum position of the cuvette was determined, we evaluated the change of the beam width as a function of the incident power P; the results are presented
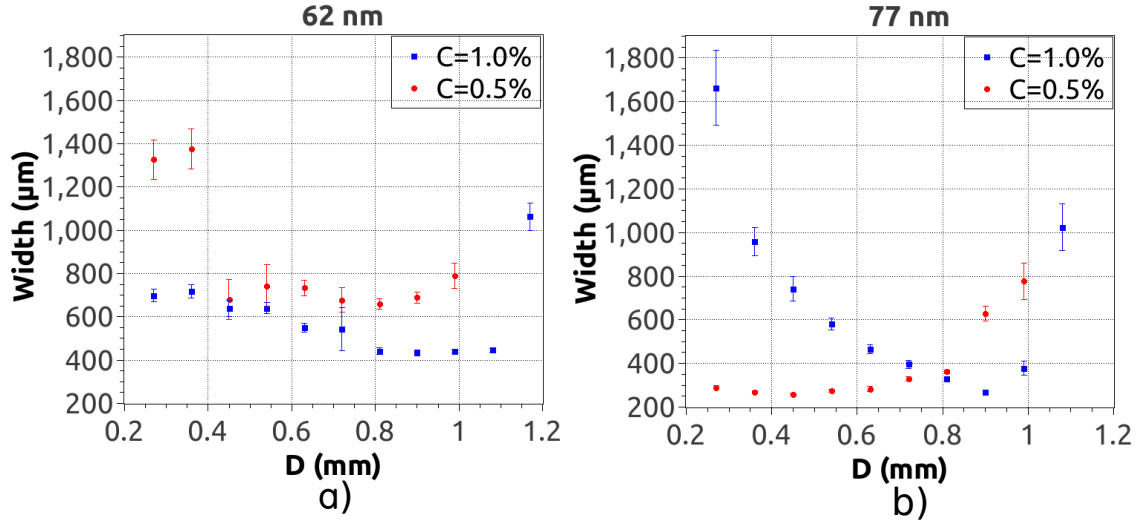
Figure 2.7: Width of the output beam as a function of the distance D between the sample and the microscope objective for the samples with particles of: (*a*) 62 *nm*-diameter, and (*b*) 77 *nm*-diameter, for the two analyzed concentrations in each case. The incident power was kept fixed with a value of 0.6 W.

in Fig. 2.8. As seen from the figure, the beam width decreases monotonically for all the cases except for the sample with 77 nm-particles at $C = 1\%$, for which the width reaches a minimum and then starts increasing. According to the z-scan curves, this sample exhibits the smallest change in the nonlinear refractive index, while it has the largest nonlinear absorption. In fact, as we shall see, the beam obtained in this case becomes very unstable *i.e.*, the cross section increases intermittently (see appendix A) as the power is raised. For this reason, data for $P > 1\ W$ is not shown in the figures. This behavior was attributed to an increase in temperature of the medium due to the larger linear extinction and nonlinear absorption observed in this sample. Regarding the other samples, the most stable soliton with a narrow cross section was observed for the colloid with 62 nm-particles at 1%, which is consistent with the z-scan curves, since this showed the maximum nonlinear response. Although

the colloid with 77 *nm*-particles at 0.5% allows for the propagation of an *OSS* of smaller cross section, it also becomes unstable as the power increases.
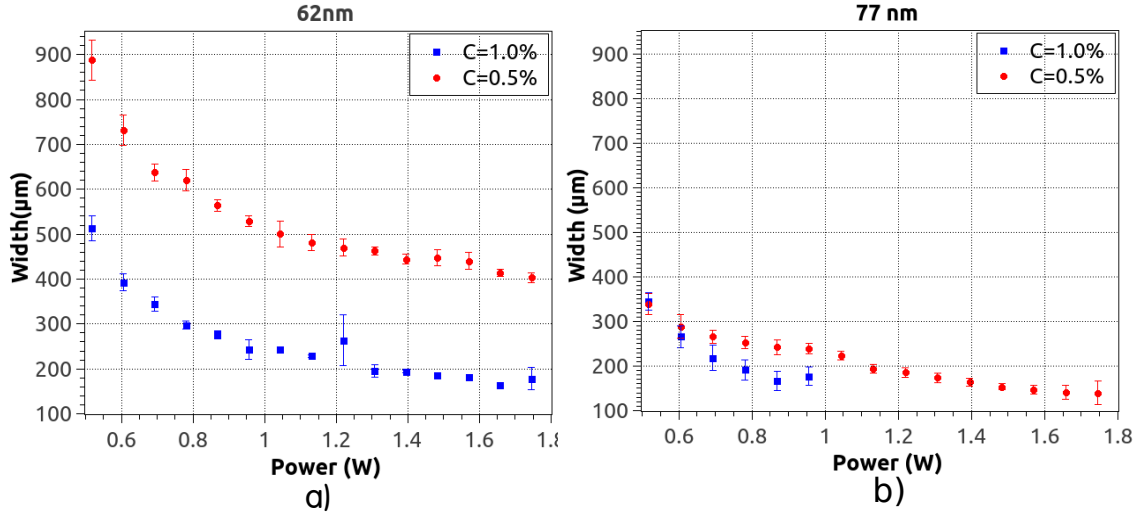
Figure 2.8: Width of the output beam as a function of the incident optical power for the samples with particles of: (*a*) 62 *nm*-diameter, and (*b*) 77 *nm*-diameter, for the two analyzed concentrations in each case.

2.3   Temporal stability of OSS

Concerning the stability of the solitons obtained in the different samples, we noticed important differences for the particle sizes used in the colloids. Specifically, the samples with 77 *nm*-particles become unstable for large values of the incident power, apparently due to thermal effects. To illustrate the instability in the temporal evolution of the *OSS*, an image was composed by stacking the registered beam profiles over the total duration of the video (2.5 *s*). This representation is shown in Fig. 2.9: the beam width is represented on the x-axis in terms of the pixel position within the images, and time scale is represented on the y axis. Further details about

this analysis are mentioned in Appendix A. The images from the samples with a concentration of 1%-solids for different values of the incident power, indicated at the top of the figure, were analyzed with this procedure. The top and bottom rows corresponds to the colloids with 62 *nm*-particles and 77 *nm*-particles, respectively. From these images, it is seen that the beam becomes narrower and very well defined in the former case as the power increases. In contrast, the beam is hardly defined in the latter case for $P = 0.953\ W$, and it has completely disappeared for higher laser powers. The "grainy" aspect in these graphs indicates changes among consecutive images caused by rapid variations in intensity, resulting in noisy intensity profiles.
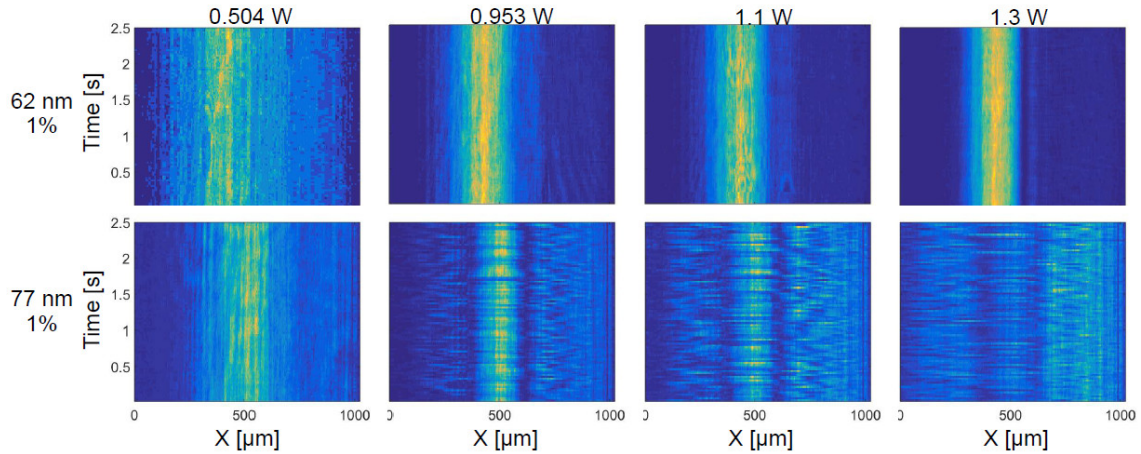
Figure 2.9: Temporal evolution of the cross section of the output beam for different incident powers indicated on the top, for samples with nanoparticles of 62 *nm* (top row) and 77 *nm* (bottom row), for a concentration of 1% solids. Dark blue corresponds to zero intensity, while yellow correspond to the maximum intensity.

2.4   Response time of samples

We also explored the response time (rt) of the samples, defined as the time at which the width of the output beam reaches a minimum size for a fixed optical power. For this purpose, we analyzed several videos of the output beam taken at a frame rate of 50 fps. A typical curve from these measurements is shown in 2.10, along with examples of the beam profiles recorded with the CCD camera for three different times (denoted as A, B and C). The response time for all the tested samples was of approximately 1 second, which can be considered fast when compared to other materials showing self-focusing effects such as photorefractive crystals ($rt = 10^2$ seconds [71]) or nematic liquid crystals ($rt = 25$ seconds [18]).
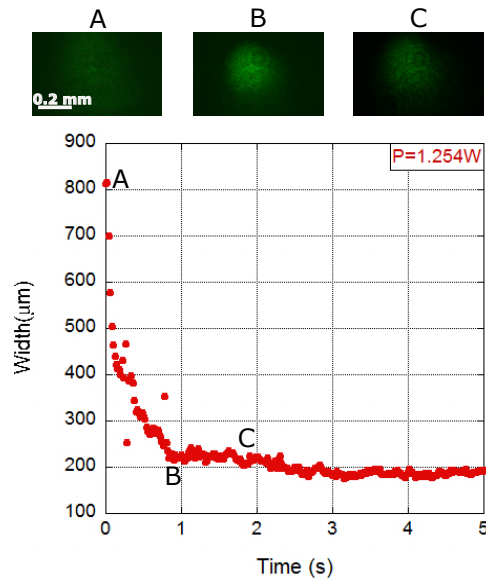
Figure 2.10: Width of the output beam as a function of time. The sample was formed by particles of 62 nm diameter and $C = 1\%$, $D = 1\ mm$ and $P = 1.2\ W$. The insets on the top, labeled as A, B and C, correspond to points illustrated in the plot.

2.5 Discussion

The results presented here, demonstrated that concentration and particle size parameters change the nonlinear optical response of nanocolloids. Z-scan analysis does provide a useful insight on the conditions favoring the formation and propagation of solitons in this type of nanocolloids. Because of the experimental conditions used in this work, none of the available models describing nonlinearities in colloidal media were suitable for fitting the experimental curves. For all samples we obtained a positive nonlinear response, the results suggest a nonlocal character on the response of the colloids.

From the results of Z-scan analysis and OSS formation and propagation, we can make a the following summary: Among the analyzed samples, we found that the colloid with 62 nm-particles at a concentration of 1% showed the maximum change in the nonlinear refractive index, followed by the same type of colloid at a concentration of 0.5%. In contrast, the samples with 77 nm-particles have the largest nonlinear absorption, attributed to accumulation of particles the larger linear optical absorption but also to scattering.

As observed in the experiments of OSS formation, some instabilities appears due to thermal effects, which can induce particle motion and redistribution. In fact, some particle aggregates were observed after using the same sample for long periods of time (more than one day). For this reason, each experiment involving OSS propagation required the preparation of a fresh sample. This observations pose important questions about the life time of the colloids. In general, vendors do not

provide an expiration date for these kinds of samples. We briefly explore the integrity of the colloids by testing their nonlinear optical properties with the Z-scan technique after 18 months. The curves in Fig. 2.11 show the results of this experiment. For colloidal suspensions with 62 nm particles, the curves are asymmetric and exhibit the characteristic nonlinear positive response. However, the amplitudes of ΔT_{v-p} are smaller than before. If we called ΔT_1 the first results of Z-scan (see page 40, Fig.2.3) and ΔT_2 the measurements realized 18 monts later, we can observe differences. For example, $\Delta T_1 = 2.25$ in the first set of measurements, whereas $\Delta T_2 = 1.65$ for the measurements obtained 18 months later. Regarding the concentration, for $C = 0.5\%$ the amplitude of the transmittance curve is smaller than the one registered for colloid with $C = 1\%$, showing a $\Delta T_1 = 1.5$ and a $\Delta T_2 = 1.2$. These differences in amplitude are attributed to the formation of aggregates in the colloidal suspension, confirming that the samples indeed suffer some degradation. Nonetheless, for both cases we can still obtain the same nonlinear response and the influence of concentration and, particle size are still evident.

For all cases, the response time of the colloids was 1 second. Because this time is lower than those reported for other materials (photorefractive crystals and nematic liquid crystals), this finding could be relevant for exploring soliton interactions and soliton-induced wave guides [8]. Both of these applications are explored in the following chapters. In particular, we investigate the use of fluorescent particles in nanocolloids, aiming at evaluating the feasibility to guide the fluorescence through an *OSS*-induced waveguide.

Perhaps the most important result from these experiments is related to the propaga-
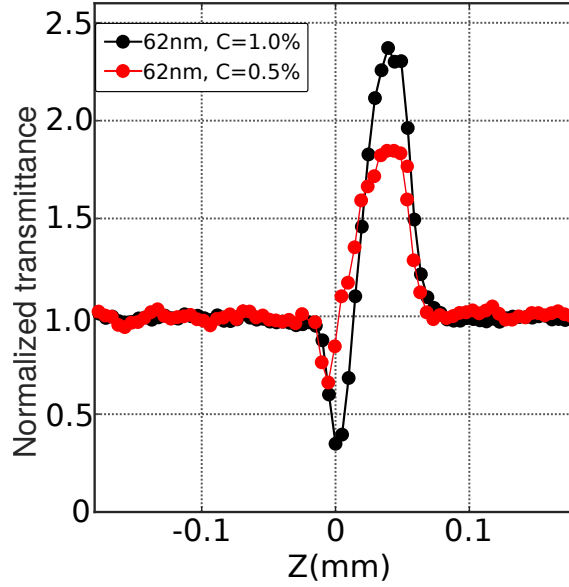
Figure 2.11: Normalized transmittance curves of close-aperture scheme. This plot shows the results obtained 18 months later in comparison with Fig. 2.3 *a*. The transition valley-peak indicates a positive nonlinear response and the difference is because of the degradation of the sample.

tion distances of OSS in these media. Our experiments show that soliton beams can propagate in these nanosuspensions over distances that are one order of magnitude longer than those previously reported for media with $\alpha > 0$ [1]. These distances are actually comparable to those reported for media with $\alpha < 0$.

These results can be understood as follows. First, it is important to remember that the gradient force, which is responsible of the self-focusing effect by attracting the particles to the highest intensity region, is proportional to a^3 (with a is the radius of the particles). In contrast, the scattering force that pushes the particles in the propagation direction, which may cause instability of the OSS due to an increased motion of the particles, is proportional to a^6. If we consider the ratio of the gradient force to the scattering force, R, as defined in Eq. 1.38 (section 1.2.4),

we can conclude that a larger value of R (smaller particles) implies a more stable OSS. The range of particle sizes studied in previous works were in most cases larger than the range studied here (see Table 2.1 for some comparative values). There is just one case, in reference [1], of a sample with smaller particle size of 38 nm and therefore a larger R. However, if we compare only the gradient forces, these are 4.3 times larger for our particles of 62 nm, giving rise to a higher nonlinear response. Then, we used an unexplored particle size range, which seems to be the optimum.

d (nm)	R
This work	
77	1.55
62	2.98
57	3.83
Ashkin [1]	
38	12.94
88	1.16

Table 2.1: Comparison of particle radii and the R factor calculated with Eq. (1.38) for different experiments.

Accordingly, the OSS formed with the sample using 62 nm-particles and $C = 1\%$ yielded the largest propagation distances for OSS. For this sample, the propagation distances of the solitons reached the full-length of the cell (6 mm). Meanwhile, in the sample with 77 nm-particles and $C = 1\%$, the OSS propagated along similar lengths; however, these beams exhibited strong instabilities as the power was increased, presumably due to strong thermal effects. Sample heating induces self-defocusing of the beam thereby affecting the stability of the OSS at higher optical power ($P = 1$ W or more).

Soliton Beams in a colloid with a mixture of fluorescent and transparent nanoparticles

Effects leading to the formation of OSS in colloidal suspensions can be classified in two general classes: effects relying on the optical gradient force [1, 23–25, 72], and thermal effects relying on the absorption, either in the fluid or in the particles [73,74]. Therefore, the optical gradient force and thermal effects play an important role in the interaction between light and nanosuspensions. While the gradient force induce the self-focusing effect, thermal effects produce self-defocusing because of the heating of the suspending media.

As shown in the previous chapter, OSS can be formed in samples with non-absorbing particles. Previous reports have also shown that OSS can readily work as a waveguide for beams propagating in colloidal media [8]. These findings have lead to the demonstration of random laser emission generated in nematic liquid crystals guided by an OSS [75]. The advent of fluorescent particles therefore suggest that an OSS

propagating in colloidal media with these particles could also lead to fluorescence guidance within the path of the OSS. In this chapter, we explore the effects observed when a colloid with a mixture of fluorescent and non-fluorescent nanoparticles are used to generate an OSS.

3.1 Generation of OSS in fluorescent nanocolloids

The experiments described in this chapter were carried out using colloidal suspensions with a mixture of both, fluorescent (60 nm diameter) and non-fluorescent (62 nm diameter) nanoparticles. Two suspensions were prepared for these experiments, both with a concentration $C = 1\%$ of solids of the total volume, but with different concentrations of fluorescent particles (C_f). Initially, we started with a sample having concentration of $C_f = 0.2\ C$, selected to obtain an adequate fluoresce signal. As discussed below, this sample showed significant thermal effects and we therefore decided to reduce the concentration of fluorescent particles to $C_f = 0.01\ C$ for the second sample.

The setup used to generate spatial optical solitons in the colloidal suspensions was the same as that described in chapter 2 (Fig. 2.1). In this case, however, the same light beam ($\lambda = 532\ nm$) used for generating the OSS serves as a pump beam for the absorbing nanoparticles. We used the same visualization systems described in chapter 2 (front-view system and top view camera). Some results obtained with colloids formed with non-absorbing particles (62 nm) were used as a reference, serving as a "control sample". A typical OSS formed in this nanocolloid

is included in Fig. 3.1, showing the images obtained with the top and front view of the cell. As before, each camera allows for observing the propagation of the beam through the glass cell ($L = 6\ mm$) Fig. 3.1 (a) and its cross-section (b). All the images were obtained from videos of the top and the cross section of the OSS; there were analyzed using the same image analysis procedure described in Appendix A. As before, this analysis yields the size of the cross section of the output beam.

(a)	(b)
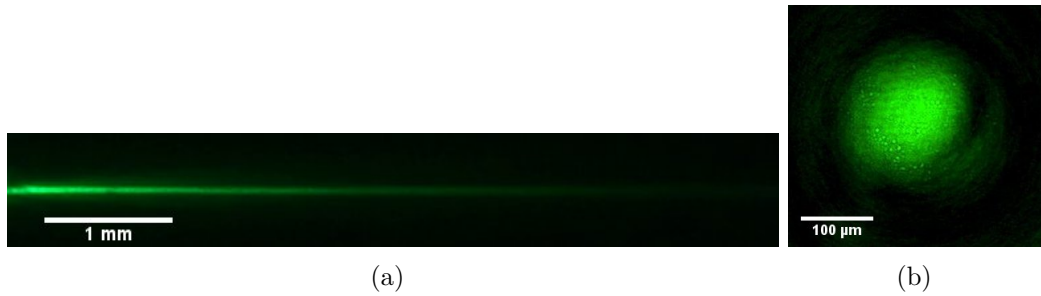
Figure 3.1: Photographs of a soliton formed in the colloidal suspension with $62\ nm$ particles, the power was 1.22 W, (a) top view, soliton propagation, and (b) cross section photograph of the soliton.

With the data obtained from the image analysis we obtained the width of the OSS as a function of the pump power. As described in the previous chapter, the optimum laser power required to generate the OSS was determined upon measuring the width output beam. Figs.3.2 and 3.3 show the width of the beam at the output of the cell as a function of the pumping power for the two samples. A first thing to note from the figures is that the beam widths obtained when decreasing the optical power seem to differ slightly from those obtained when the power was increased. Such behavior therefore suggests that the nanocolloid with absorbing (fluorescent) particles presents a hysteresis effect.

Both graphs were fitted with a second order polynomial curve in order to gain a
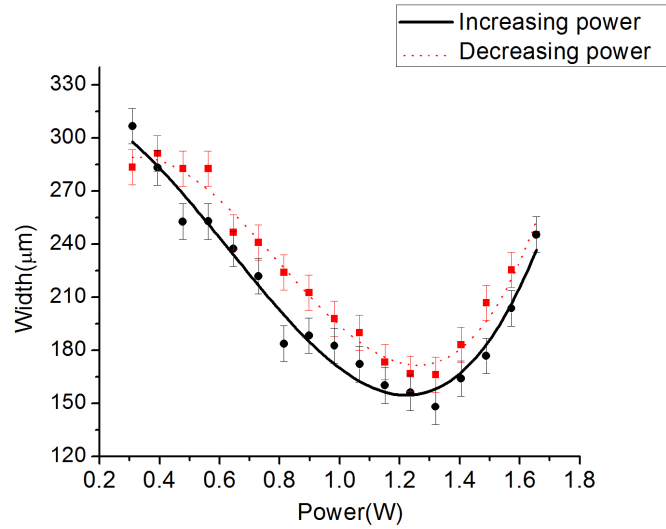
Figure 3.2: Width vs power of the sample with $C_f = 0.01\ C$.
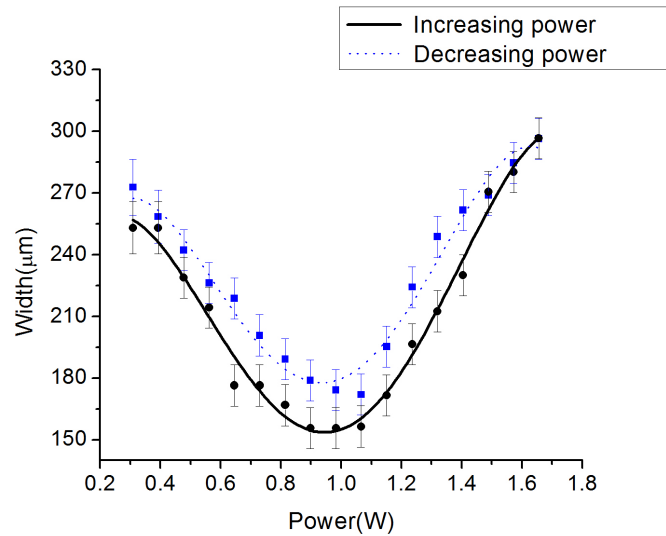
Figure 3.3: Width vs power of the bi-dispersed sample with $C_f = 0.2C$.
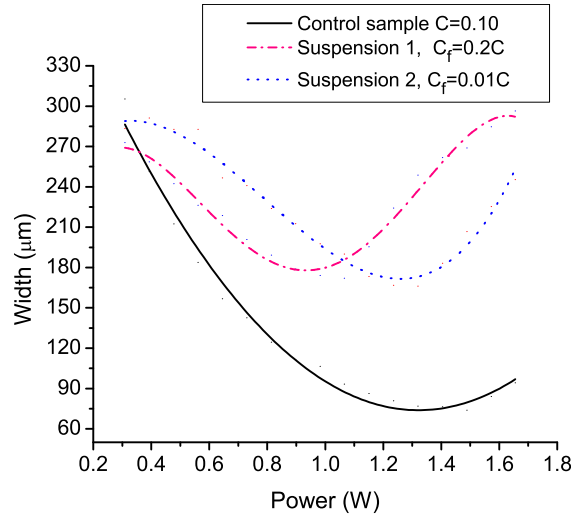
Figure 3.4: Curves of the cases when a sweep of power form 0.44W to 1.75W was made. Black solid line is represents the width change as a function of input power, notice that the width increases slightly at powers bigger than 1.3 w. Dash pink and blue lines describes the colloids with fluorescent particles ($C_f = 0.2C$ and $C_f = 0.01C$, respectively). In these cases the width grows more than in the case of "control sample".

better insight of the pump powers required to achieve the minimum width in the OSS. For the low concentration fluorescent nanoparticles ($C_f = 0.01\ C$), the power for minimum width was $1.22\ W$, which is the same power required to obtain a minimum cross section size in samples with non-absorbing particles of $62\ nm$. In contrast, for the case of the nanocolloid with $C_f = 0.2\ C$, the power required to obtain a minimum cross-section is around $0.95\ W$. Other important observations include temporal instabilities in the OSS in both samples, particularly when compared to those obtained with non-absorbing colloids. We attributed this to the thermal effects induced by the absorption of the fluorescent nanoparticles and also to the formation of microbubbles produced when filling the cell.

A comparison of the width of the OSS obtained with both samples, including the

"control sample" is shown in Fig. 3.4, obtained while the pumping power was increased. Notice that the OSS formed in the control sample are significantly narrower than the beams obtained in the media with absorbing particles. Further analysis of the cross-section of the OSS revealed the formation of a pattern of rings around the main spot of the output beam, as shown in Fig. 3.5. Although the rings were also observed in the control sample (monodisperse non-fluorescent colloid), these were considerably less in number, intensity and sharpness. In fact, for the sample with a large concentration of fluorescent particles, a larger number of rings were observed. In all cases, the output patterns were non-symmetric: they were better defined in the upper region of the image than in the lower region, this is attributed to the convection flow. Although further work is needed to elucidate the origin of these rings, we believe they are caused by shedding of radiation away from the self-collimated beam. This shedding effect has been considered in experiments involving OSS interactions [9] and will be discussed in the following chapter. As for the asymmetry in the observed output patterns, these might be due to thermal convection effects, which were observed in the experiments and become more evident in samples with absorptive particles.
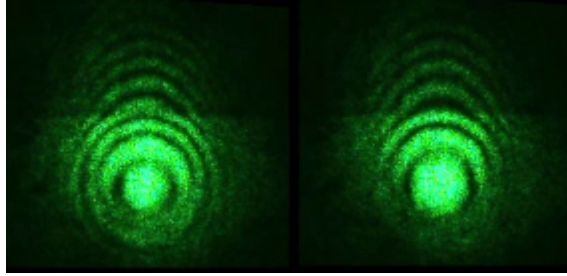
Figure 3.5: Transversal section of a soliton formed in a mix solution with $Cf = 0.2$ C; pumping power $1.22\ W$ in both photographs.The left photo was taken when the power is increasing, while the one in the right is a soliton formed when the power is decreasing. A difference in the size of the beam is observed.
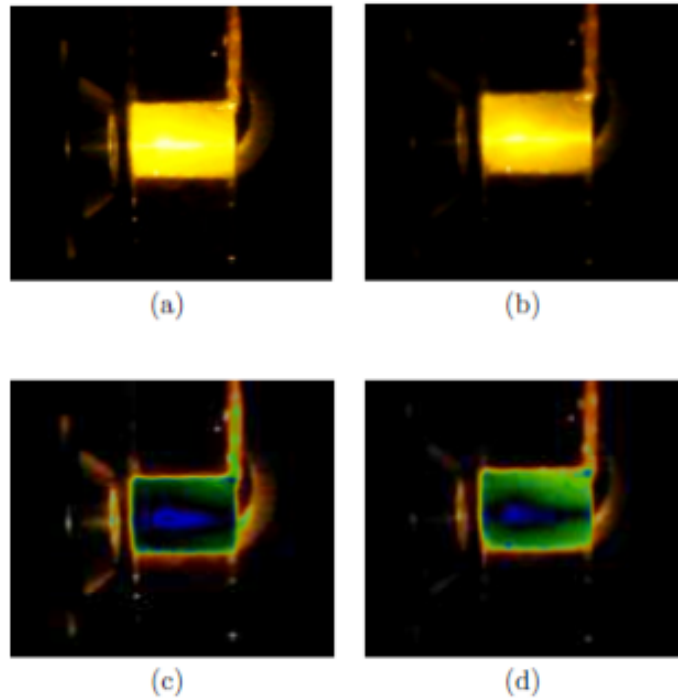
Figure 3.6: Photographs of the beam's top view using $1.22\ W$ power. In (a) and (c) the power is increasing. In (b) and (d) the power is decreasing. In the images (c) and (d) the solarize filter [75] was applied.

The images acquired with the top view camera allowed us to analyze the florescence

of the bidisperse samples for different pumping powers. In particular, the images shown in Fig. 3.6 were obtained for the same pumping power ($1.22\ W$) but under different conditions: while $3.6(a)$ and $3.6(c)$ were acquired as the power was increasing, $3.6(b)$ and $3.6(d)$ were acquired as the power was decreasing. Notice that $3.6(a)$ seems to yield a more intense and uniform fluorescence throughout the sample compared to that shown in $3.6(b)$. This difference can be further noticed upon applying digital filtering [76] to the images (see $3.6(c)$ and $3.6(d)$), such that the darkest areas now correspond to the highest density of fluorescent particles. Hence, it can be seen from Fig. $3.6(d)$ that after some time of exposure to the pumping beam, a constrained region within the cell shows a stronger fluorescence. Although further experiments s are required to fully understand this phenomenon, it might be associated to the hysteresis effect, and also, a difference in the scattering force exerted on the two kinds of particles present in the sample (fluorescent and non-fluorescent). The self-focusing effect is undoubtedly present and the reduction in the size of the beam becomes apparent from the front images, as verified from Figs. 3.2, 3.3 and 3.4. It is difficult to assess whether the beam width remains indeed constant as a function of the propagation distance. The strong fluorescence, even for the lowest concentration of fluorescent particles, prevents us to clearly observe the OSS, which must look like a filament from the top view.

3.2 Discussion

We studied the propagation of intense light beams in two different samples, which contained a mixture of non-fluorescent and fluorescent nanoparticles. In all cases, we observe a self-focusing effect and solitons formation.

The presence of florescent particles produces important thermal effects due to absorption, which lead to an increase in the minimum size of the OSS with respect to the samples with non-absorbing particles sample (chapter 2) and reduces its stability. We also observed a pattern of concentric rings around the central core in the cross-section of the OSS in all the cases, but the number and definition of the rings is higher for the fluorescent samples. This is attributed to radiation shedding of non-trapped light. More importantly, we found a hysteresis effect in the fluorescent samples; the width of the emerging beam as a function of pumping power is always smaller when the power is gradually increasing than when it is decreasing. Is this due to a degradation of the sample? Is it due to a temperature increase? Or is it owed to an uneven distribution of the fluorescent particles observed as a function of time? These are questions yet to be answered. At the moment, radiation pressure effects are being investigated in order to verify whether the changes in the distribution of fluorescent particles are produced upon varying the concentrations (C and C_f) and/or the size of the non-absorptive particles.

In the context of our work, thermal effects alter the stability of OSS. When the particles are much smaller than the optical wavelength, the gradient force is very weak; hence, a high density of particles is required to produce a significant change

in the refractive index to trap narrow beams. However, at higher particle densities, multiple scattering becomes dominant, randomizing the direction of scattered light [72].

Steering and switching of soliton beams via interaction in a nanocolloid with positive polarizability

As it was mentioned in the introduction, among the main motivations for the study of solitons are their envisioned applications in information transmission. In this context, soliton interactions might be very relevant, for example, to perform tasks like beam splitting, beam combining, and multiplexing. For this reason, this chapter is dedicated to the study of incoherent interactions of two solitons in a nanocolloid with positive polarizability, as those investigated in chapter 2. We describe two different regimes for the interaction of the solitons in $(2 + 1)D$, which are induced with orthogonal polarizations. We identify two interaction regimes, called steering and switching, which depend on the power balance and the angle between the input beams. A transition regime is also characterized.

We start with an overview of soliton interactions, including the difference between

the coherent and incoherent cases. After that, a detailed description of the experimental setup and the main control parameters is provided. Then, the interaction regimes observed in the experiments are described, and finally, the discussion of experimental results is presented.

4.1   Soliton interactions

Collisions between solitons are perhaps one of the most fascinating features of soliton phenomena because the interacting wave-packets (self-trapped beams) exhibit many particle-like behaviors [15]. Since solitons interact like particles, their interactions can be called collisions.

In general there are two interaction categories: coherent and incoherent. Coherent interactions occur when the nonlinear medium can respond to interference effects that take place when the beams overlap. Therefore, the relative phase between the beams ϕ_{rel} plays a crucial role in the general collision characteristics [77]. Coherent collisions of Kerr solitons are fully elastic, which implies that the number of solitons is always conserved [77], but the phase is shifted.

In order to obtain coherent interactions, the nonlinear response of the medium should be extremely fast [15]. For slow-response time materials, such as photorefractive crystals, the relative phase (ϕ_{rel}) between the interacting beams must be kept stationary on a timescale much longer than the response time of the medium [77]. The role of ϕ_{rel} is crucial to determine whether an interaction becomes attractive or re-
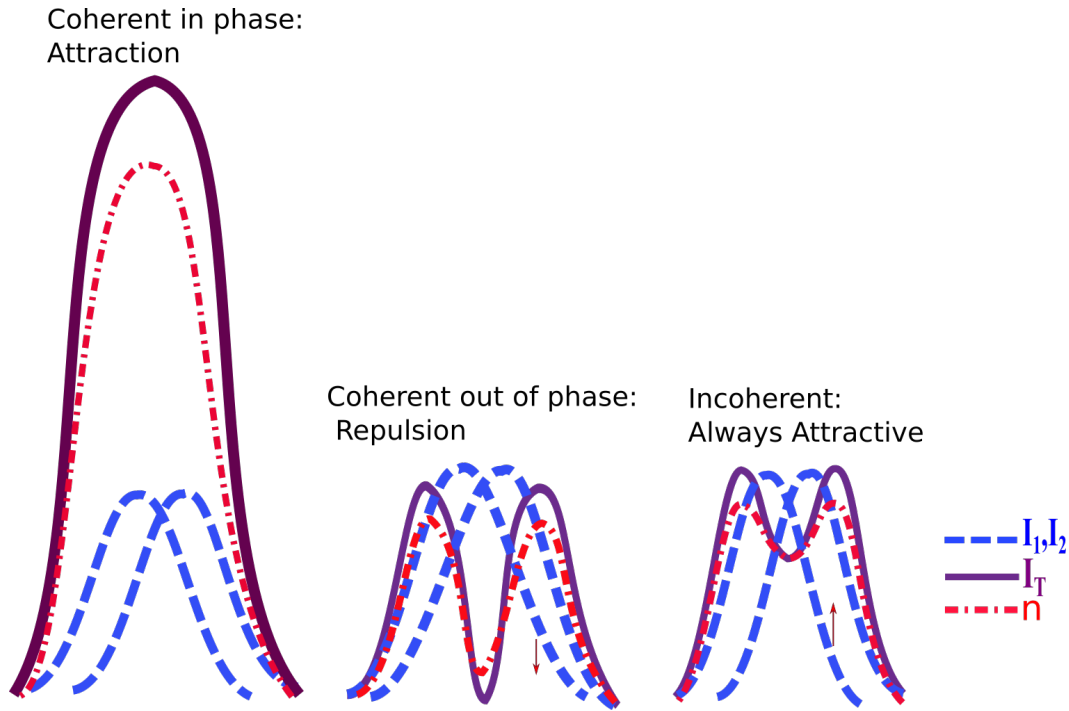
Figure 4.1: Intensity profiles of two interacting solitons (dashed lines), intensity of the superposition (solid line), and refractive index (dash-dotted line).

pulsive [78]. When the beams are in phase ($\phi_{rel} = 0$), the total intensity in the central region increases leading to an increase of the refractive index (see Fig. 4.1, left). Consequently, more light is attracted into this region and the centroids of the solitons start moving towards each other, which corresponds to the attractive force. If $\phi_{rel} = \pi$ the interference between the beams is destructive and the refractive index in the central region decreases, so the solitons repel each other [77] (see Fig. 4.1, center).

Incoherent interactions, on the other hand, occur when the relative phase between the solitons varies much faster than the response time of the material. Thus, incoherent solitons do not produce interference. The resulting intensity within the

material is approximately equal to the superposition of the intensities of the two individual components (see Fig. 4.1, right). As a consequence, the force between such solitons is always attractive [79] and might give rise to solitons fusion [77].

Experimentally, soliton interactions in $(2+1)D$ have been observed in Kerr-like materials, such as photorefractive crystals [38] and nematic liquid crystals [80]. In colloids, this kind of interaction has also been investigated. There are theoretical works on the interaction between $(1+1)D$ solitons in nanocolloids with $\alpha > 0$ [43], and $(2+1)D$ solitons in colloids with mixtures of nanoparticles with $\alpha > 0$ and $\alpha < 0$ [81]. An experimental and theoretical study on the coherent interaction between two solitons in $(2+1)D$ in a nanocolloid with $\alpha < 0$ was also carried out, where the phase-dependent behavior was demonstrated [82]. In the next section we will describe the first investigation on incoherent interactions in nanocolloids with $\alpha > 0$.

4.2   Experimental setup

For these set of experiments, we use a suspension of polystyrene nanospheres with mean diameter of 57 nm in water, with a concentration of 1% solids. This is very similar to the optimum sample characterized in chapter 2. The suspension is contained in a sealed glass cell with dimensions of 2 mm-depth $\times$ 12 mm-long. Notice that this cell is larger than the one used in chapters 2 and 3 (2 mm-depth $\times$ 6 mm-long).
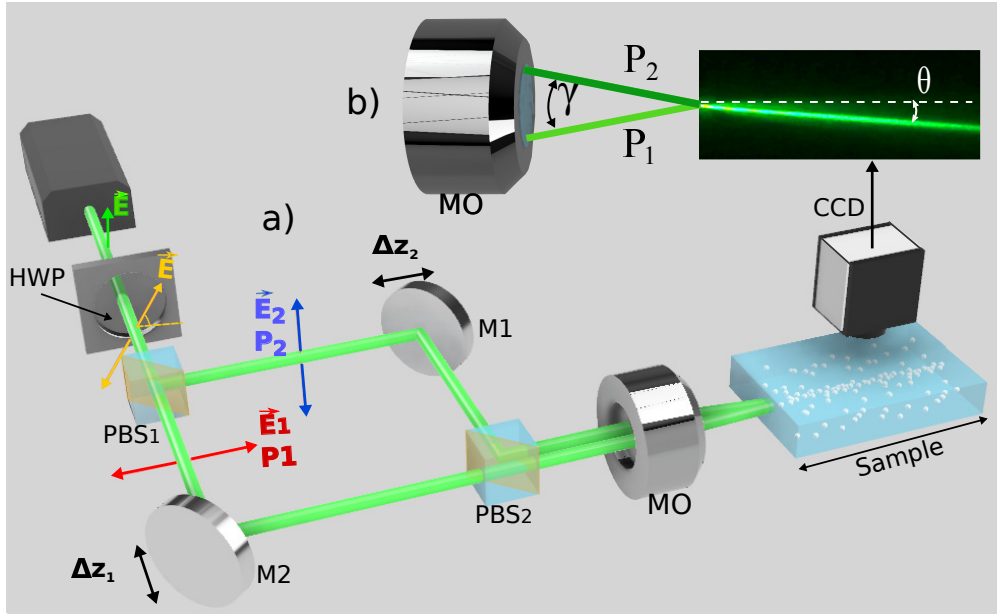
Figure 4.2: (a) Experimental setup (not to scale). The power in each beam is denoted by P_1 and P_2, and it is controlled by rotating a half-wave plate HWP. The displacements of the mirrors $M1$ and $M2$ (Δz_1 and Δz_2) control the separation between the parallel beams entering the microscope objective, determining in turn the interaction angle γ within the sample. (b) The two input beams are symmetrically displaced with respect to the optical axis, forming an interaction angle γ. The angle of the output beam, when it is formed, is denoted by θ.

The experimental setup to study the soliton interactions is shown in Fig. 4.2(a). A vertically-polarized Gaussian beam from a CW laser (532nm-wavelength) passes through a half-wave plate (HWP), which rotates the polarization plane of the input beam. Then a Mach-Zehnder interferometer is built to produce two parallel beams. The interferometer consists of a polarizing beam splitter (PBS) to separate the beam into two orthogonally polarized components ($B1$ and $B2$), which allows us to study incoherent interactions, since the beams will not interfere. The power of the corresponding beams, P_1 and P_2, is controlled by rotating the HWP. It is worth noticing, however, that P_1 and P_2 are not independent from each other, but one of

them is proportional to $\sin^2(2\delta)$ while the other is proportional to $\cos^2(2\delta)$, where δ represents the angle of the HWP axis with respect to the incident polarization. Two mirrors mounted on single-axis translation stages allow us to displace each beam independently, while keeping parallel trajectories. The mirror displacements are denoted as Δz_1 and Δz_2 for mirrors $M1$ and $M2$, respectively. A second PBS directs the parallel beams towards the microscope objective (MO), which focus them into the sample cell. A camera images the sample cell from the top. A quarter-wave plate (not shown) is placed before the MO to produce opposite circular polarizations, in order to observe the scattered light produced by both beams. This is important because the light scattered by the nanoparticles approximately obeys a dipole radiation distribution with the axis of the dipoles aligned with the incident polarization, meaning that a beam with vertical polarization will look much less intense than the horizontally polarized one when observed from the top, regardless of their relative powers.

As shown in Fig. 4.2(b), for the interaction experiments the two beams are shifted symmetrically with respect to the optical axis before the MO input. When the beams pass through the MO they form an angle γ, which we will refer to as the interaction angle. As this is a very important control parameter, the characterization of γ will be explained in detail in the next subsection. As we shall see, the two solitons fuse into a single output beam, which forms an angle labeled as θ with respect to the optical axis: this is the output variable.

In summary, the control parameters of the soliton interaction experiments characterized in this work are: the angle γ and the relative power of one of the two beams

(P_1/P_T or P_2/P_T, with $P_T = P_1 + P_2$). For the interaction experiments, a value of γ is chosen and fixed, while we study the effects of changing the relative power between the beams. We repeat this process for different values of γ.

4.2.1 Characterization of the interaction angle

In order to characterize the interaction angle γ, we will begin by characterizing the angles that each of the input beams, separately, form with respect to the optical axis as a function of the displacements of the mirrors, which are denoted by θ_1 and θ_2. For this purpose, an initial alignment was performed to guarantee that both beams enter collinear impinging at the same point, centered with respect to the MO. This configuration is considered as the reference position of the mirrors ($\Delta z_1 = \Delta z_2 = 0$) in the Mach-Zehnder interferometer. From this reference position, each mirror is moved within a range such that the beam sweeps the back aperture of the MO, whose diameter is 7 mm, 3 times larger than the spot size of the beams (2.35 mm diameter). It is important to assure that the beams are completely included within the aperture of the MO to avoid power losses. As the beam $B1$, for example, is shifted by changing Δz_1 to both sides of the reference position, its angle at the output of the MO changes in consequence. Fig. 4.3 illustrates the steering of beam $B1$ as mirror $M1$ is displaced. We can achieve a maximum angular deviation of up to $\pm 12°$ for each beam, but for the interaction experiments we will restrain it to $\pm 7°$ in order to prevent beam aberration for large output angles, as we will explain in the next section.
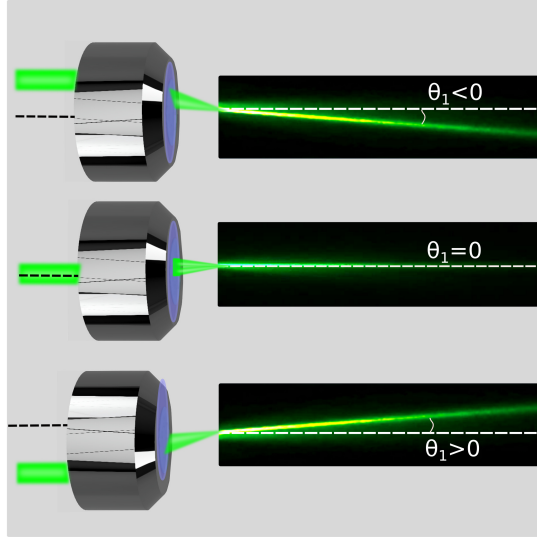
Figure 4.3: Steering of the beam $B1$.

The angle θ_1 or θ_2 is measured when the corresponding beam is inside the sample and the soliton is formed. We set the maximum power for the beam that is being characterized, $B1$ for instance, while the power of $B2$ is minimum and it is blocked to avoid any interaction contribution. We neglect the refraction of the beams at the input interface of the sample cell, since we are dealing with small angles ($-7^\circ \leq \theta_{1,2} \leq 7^\circ$). For each mirror displacement an image of the beam is captured and then analyzed. A Matlab code was developed to obtain the angle by means of a linear fit of the points of maximum intensity for each z position along the beam propagation. From the fit we obtain the line slope m, so that $\theta_{1,2} = \arctan(m)$. Fig. 4.4 shows the fitted line superimposed on the original image in pixel units. The scaling and conversion from pixels to mm is described in Appendix A. This process is repeated several times for each beam in order to obtain average values and the respective uncertainties. In Fig. 4.5, the dependence of $\theta_{1,2}$ on $\Delta z_{1,2}$ is presented.
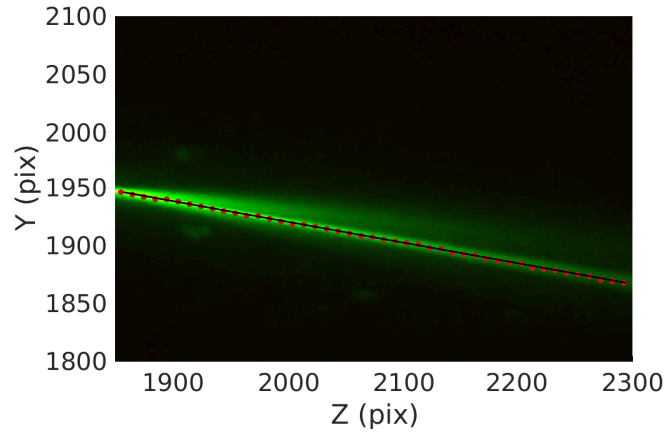
Figure 4.4: For the characterization of the input angle of a single beam, an image of the soliton induced in the sample is converted into a numerical matrix and analyzed with a Matlab code. The intensity maxima along the propagation direction (Z) are detected and a linear fit of these points is obtained, whose slope is directly related with the propagation angle. In this example, the fitted line is superimposed on the original image.
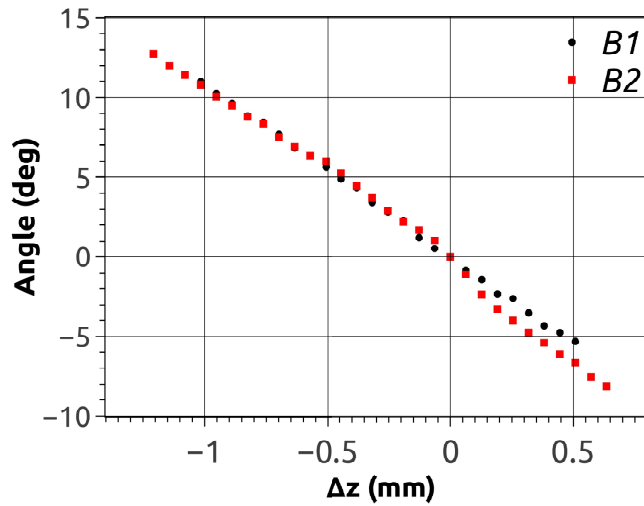
Figure 4.5: Dependence of the input angles θ_1 and θ_2 on the displacements Δz_1 and Δz_2 of the mirrors $M1$ and $M2$ respectively (see Fig. 4.2).

For the sake of simplicity, in the interaction experiments described in the next section, we set a symmetrical configuration of the beams entering the sample, such

that $\theta_1 = \gamma/2$ and $\theta_2 = -\gamma/2$, giving an interaction angle of γ. As we shall see, for small values of γ the two beams merge into a single output soliton, whose angle is labeled θ and is characterized in the same way described above.

4.3   Interaction regimes

In all cases the interaction is attractive, which is not surprising for incoherent solitons [15]. What surprises indeed, is that we observe soliton fusion for interaction angles of up to $\sim 10°$, whereas in photorefractive crystals the reported values are of the order of $\sim 0.5°$ [38, 39], indicating a much stronger interplay in the nanocolloids. Furthermore, we observe novel features when we study the interaction as a function of the power imbalance between the input beams for different values of γ. We identify two characteristic regimes and a transition behavior in-between. In what follows, the total power entering the colloid is $P_T = P_1 + P_2 = 1.2$ W, unless otherwise stated.

Regime I ($\gamma < 10°$). For small intersection angles, the well-defined single output soliton resulting from the fusion can be continuously steered as the relative power between the input beams is gradually changed, as depicted in Fig. 4.6. This can be interpreted as an inelastic collision where the two input beams become mutually trapped along a single channel, whose direction is determined by their relative initial momenta, thus bending towards the strongest beam. However, the emerging angle θ does not vary linearly with the ratio of the power in one beam to the total power, P_1/P_T, as shown in Fig. 4.7 for three values of γ, where the markers represent
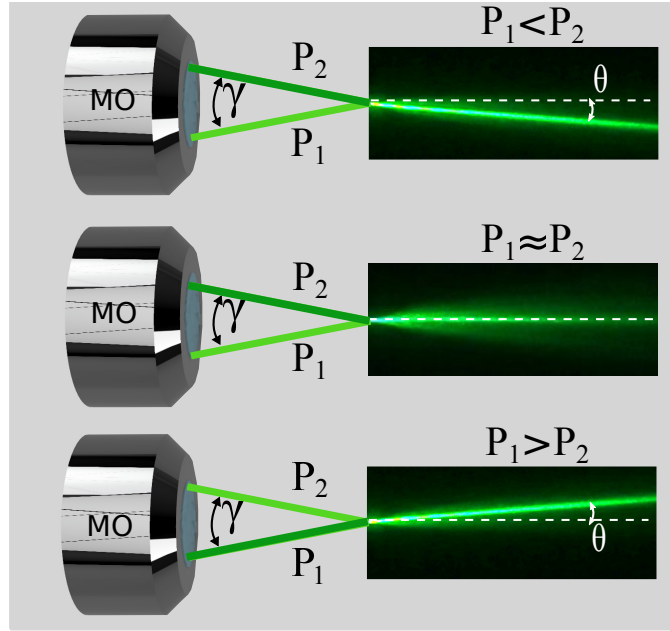
Figure 4.6: Schematic illustrating the steering of the single soliton obtained from an incoherent interaction as the relative power between the input beams is changed,for a fixed value of γ.

experimental measurements. The images on the top show the emerging soliton when $P_1/P_T = 0$ (left), 0.5 (center) and 1 (right), for $\gamma = 7°$. The output beam starts becoming ill-defined as γ increases when $P_1/P_T \sim 0.5$. The solid lines in Fig. 4.7 are the result of simulations based on a theoretical model introduced in Ref. [65], described in Appendix B, which did not form part of this thesis, but were performed in close collaboration with our colleagues Luke Sciberras and Antonmaria Minzoni.

Transition regime ($\gamma \sim 10°$). When the interaction angle reaches approximately $10°$ and $P_1/P_T \sim 0.5$, we observe an unstable oscillation of the output beam, which is no longer a soliton, but it is wider than the solitons formed for other values of P_1/P_T. We tracked the position of the centroid of the output intensity profile in this case (see Fig. 4.8) and performed a Fourier transform, but we did not find
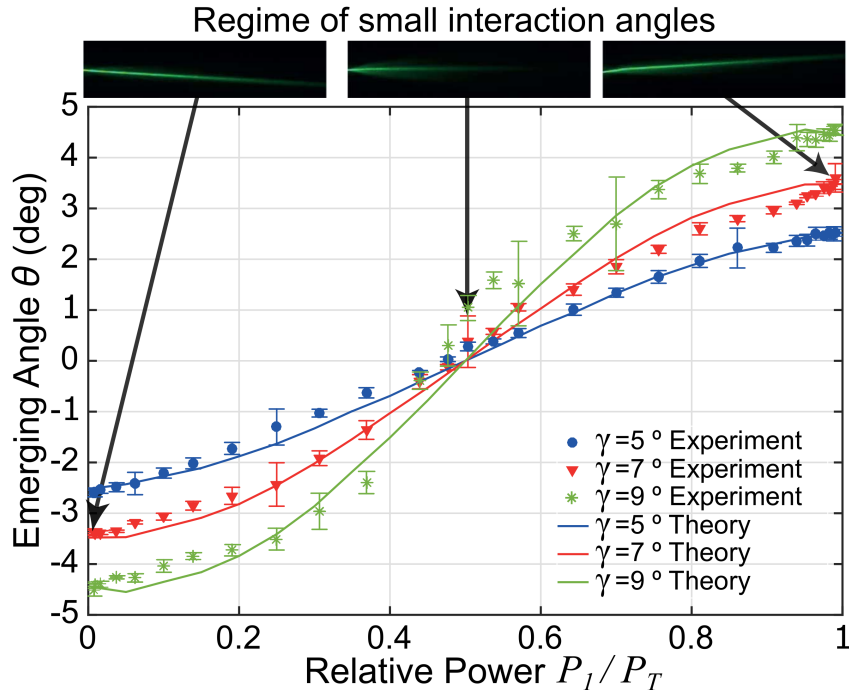
Figure 4.7: Emerging angle θ of the single output soliton as a function of P_1/P_T, with $P_T = 1.2$ W, for three interaction angles: $\gamma = 5°$, $7°$, and $9°$. Markers correspond to our experimental results, while solid lines correspond to simulations. Pictures on the top: emerging soliton when $P_1/P_T = 0$ (left), 0.5 (center) and 1 (right) for $\gamma = 7°$.

a characteristic frequency. It seems that both beams are competing to guide the light towards their respective directions whilst perturbations in the intensity due to the diffusive motion of the particles within the medium favour one beam or the other randomly. No angle can be associated to the output beam in this situation. However, a little imbalance in the relative power gives rise to a sudden formation of a well defined soliton, whose direction approximates rapidly to that of the strongest beam as the power imbalance increases. Namely, the emerging beam starts switching between its limiting positions when $P_1/P_T \neq 0.5$.

Regime II ($\gamma > 10°$). At large angles the interaction region becomes very small.
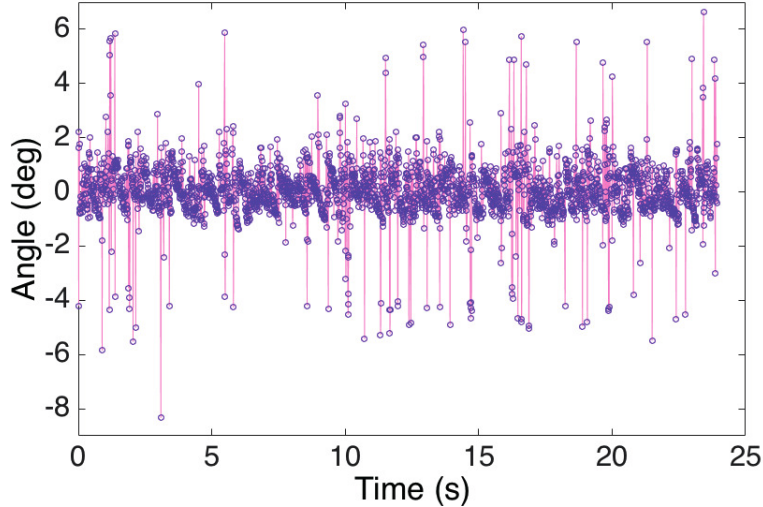
Figure 4.8: Tracking of the position of the centroid of the output intensity profile obtained in the transition regime of the interaction, when $P_1/P_T \approx 0.5$. The observed oscillations has no defined frequency when analyzed by a Fourier transform.

Now we observe two separated output beams when $0.38 \lesssim P_1/P_T \lesssim 0.62$, none of them behaving like a soliton. Nevertheless, these beams do not freely diffract either. A reduced self-focusing is observed in both beams, reaching a minimum for $P_1/P_T = 0.5$. Moreover, the output angle between the beams is smaller than input the angle, meaning that they still attract each other. There seems to be a threshold, such that when the power imbalance exceeds $\sim 12\%$, the strongest beam can form a waveguide for the weaker one, and a single output soliton starts forming again along almost the same direction of the strongest beam. This switching behavior becomes clear in Fig. 4.9, where the shadowed region represents no soliton formation. The output beams observed for $P_1/P_T \sim 0.5$ keep separated, even if the total power is increased up to 2.4 W, implying that the threshold is not associated with the power in each beam, but with its distribution. In fact, if we block one input beam, the other one becomes self-collimated and propagates along its original direction.
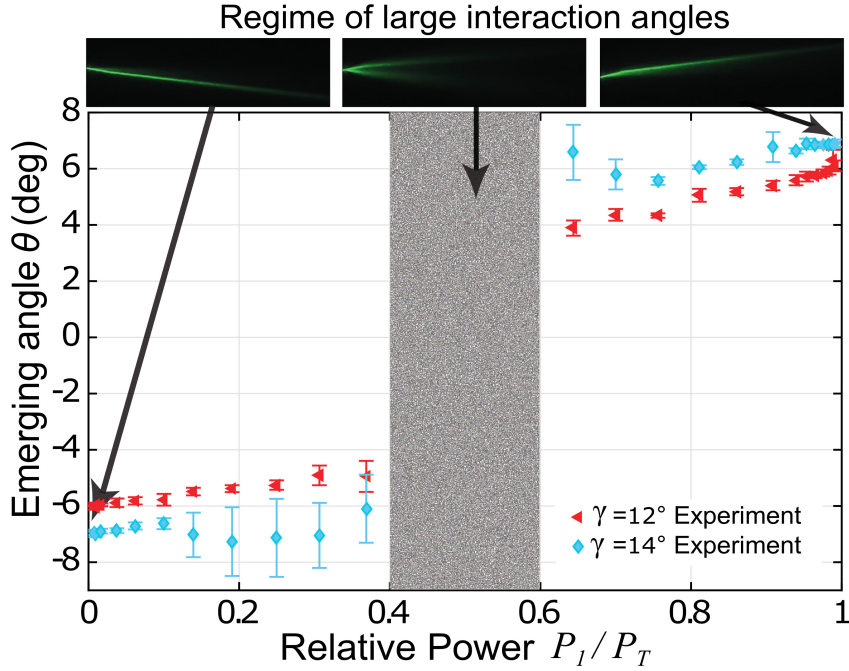
Figure 4.9: Emerging angle θ of the output beam *vs* P_1/P_T, for $\gamma = 12°$ and $\gamma = 14°$.
In the shadowed region there are two output beams. Pictures on the top: emerging
beam(s) when $P_1/P_T = 0$ (left), 0.5 (center) and 1 (right) for $\gamma = 14°$.

For characterizing the self-focusing and attraction effects of the output beams at
large interaction angles, we set $\gamma = 10.4°$ and fixed the value of $P_1 = 1.29$ W. Then
we gradually increased the power of the second beam from 0 to the same value of
$P_2 = 1.29$ W. To control the power of beam $B2$ independently from $B1$, a second
half-wave plate is introduced in this arm of the interferometer, so that only part of
$B2$ is reflected by $PBS2$ while the rest is transmitted (see Fig. 4.2).

Fig. 4.10 shows the output width of beam $B1$ (black markers, scale on the left)
and its output angle with respect to the optical axis θ_1 (scale on the right, white
markers) as a function of P_2/P_1. As P_2 increases, beam $B1$, originally self-collimated,
gets wider and changes its propagation direction within the sample, decreasing its

output angle θ_1 down to a minimum value of half its initial value when $P_2 = P_1$. This behavior has not been observed in other nonlinear media. Our hypothesis to explain this is the following: At large angles γ, the nanoparticles in the interaction region distribute between the two beams, so that there are not enough particles to produce a strong self-focusing effect in any of them.
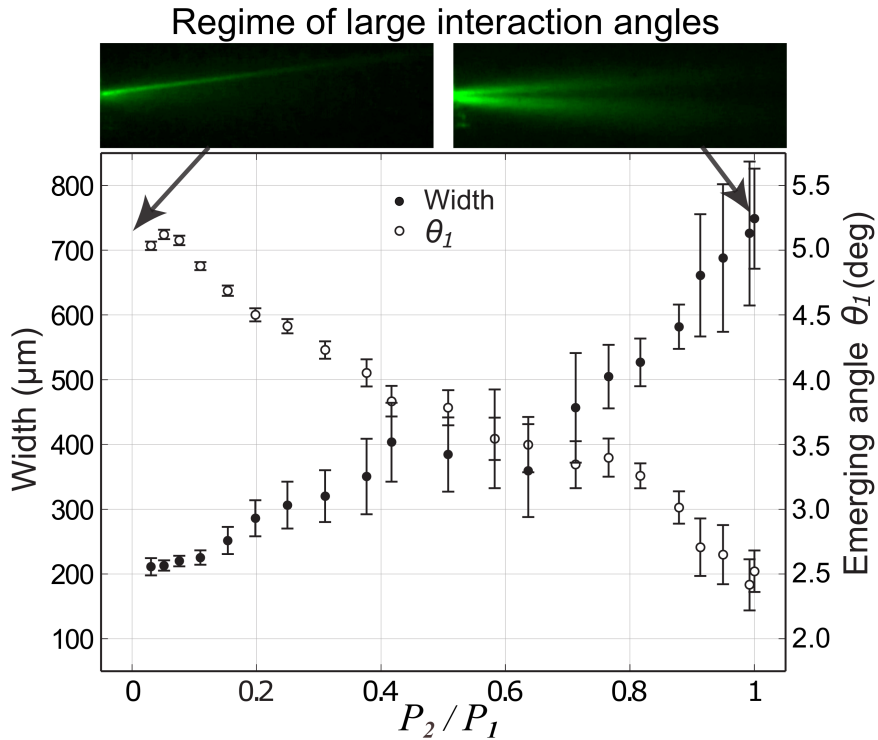
Figure 4.10: Changes in the width (black markers, scale on the left) and in the output angle θ_1 (white markers, scale on the right) of beam 1, as a function of P_2/P_1, with $P_1 =$1.29 W. Images on the top: $P_2/P_1 = 0$ (left) and 1 (right).

4.4   Discussion

In summary, we unveiled different regimes for the incoherent interaction of two solitons induced in a nanocolloid with $\alpha > 0$. It is worth to stress that soliton interactions in this medium were considered unfeasible [2, 44]. Another remarkable fact is that we were able to explore intersection angles of up to 14° and still obtain an interaction between the input beams. In other materials, like photorefractives and liquid crystals, typical interaction angles are of the order of 0.5° [38].

We presented the first experimental study of incoherent soliton interactions having the relative power between the input beams as a control parameter. For interaction angles $\gamma < 10°$, it was found that the two beams merge into a single soliton, which can be continuously steered across the whole angular range by changing the power balance between the input beams. For interaction angles $\gamma > 11°$, there is a single emerging soliton only when the power imbalance is above certain threshold, and it can be switched between two limiting positions. However, there are two output beams when the power is approximately balanced; none of them is a soliton, although they still attract each other. A transition behavior between the two regimes is characterized by a rapid oscillation of the emerging beam when the power is balanced. The steering and switching mechanisms in this medium could be applied to route additional light beams with a rapid response time. Also, our results unveil new aspects about the nonlinear optical properties of dielectric nanocolloids and soliton interactions, showing that there are still open questions.

Conclusions

In this thesis, the formation of optical spatial solitons in dielectric nanocolloids with positive polarizability was demonstrated. The propagation distance of these solitons was surprisingly large, in excess of 10 mm, although this had been considered unfeasible [2]. Moreover, the nonlinear optical response of these kinds of suspensions was characterized as a function of particle size and concentration, finding that these parameters play a crucial role in OSS formation. This was also done for nanocolloids formed by a mixture of transparent and fluorescent nanoparticles. In that case, we found that the thermal effects are predominant when the wavelength of the laser is highly absorbed by the sample affecting the stability of solitons. In addition, we studied for the first time, the incoherent interactions between two solitons in dielectric nanocolloids with positive polarizability, and found three regimes of interaction that can be used as a mechanism of beam steering or switching.

We started by analyzing the linear response of four samples of dielectric nanocolloids, with particles of of 62 and 77 nm-diameter and concentrations of 0.5% and 1%.

Our results demonstrated that these materials present low linear absorption, but it depends on particle size and concentration. The absorption is the largest in samples with particles of 77 nm at a concentration of $C = 1\%$. This fact is very important in OSS formation, because we induced them using high power ($\approx 1\ W$), so thermal effects become important.

On the other hand, we used the Z-scan technique to characterize the changes in the nonlinear refractive index and absorption of the nanocolloids. With this, we were able to identify that for all the tested samples, the nonlinear refractive curves show a positive nonlinearity, which implies that they admit the formation of bright solitons. Particle size and concentration also have a crucial influence on the nonlinear response of these media. In particular, the colloid with 62 nm-particles and a concentration of $C = 1\%$ showed the maximum change in the nonlinear refractive index and minimum nonlinear absorption. In contrast, the sample with 77 nm-particles has the largest absorption for $C = 1\%$ and the minimum nonlinear refractive response for $C = 0.5\%$.

These results are very relevant as well for OSS formation and propagation. For example, the solitons induced in the nanocolloid of 62 nm-particles are very stable on propagation over the whole length of the sample cell (6 mm), exhibiting a slight divergence at the end of the cell. The minimum sizes of solitons, were obtained in colloid with 77 nm-particles and $C = 1\%$. However, soliton instabilities appear in this case, meaning that the beam changes rapidly in time. This is attributed to thermal effects, since this is the sample with the highest linear absorption. These results are consistent with those obtained in the Z-scan study.

Once the optimum particle size and concentration have been determined, the main parameters for the OSS formation were identified and characterized: the input power and the distance between the microscope objective and sample container, D. These parameters are relevant because the colloids behave as Kerr-like media, meaning that their refractive index changes as a function of the optical power P. Also, variations in D produce a change in the size of the beam impinging on the colloidal sample, thereby changing the intensity and the wavefront of the beam interacting with the particles. Additionally, we characterized the response time of the nanocolloids in terms of OSS formation. This is of the order of $1s$, while in other materials like nematic liquid crystals the response time is about $25s$ [18] and for photorefractive crystals is of 10^2 s [71]. Therefore, the nanocolloids might be advantageous in some photonic applications. Nevertheless, we are aware that the large power levels required and the high scattering represents a disadvantage.

On the other hand, we analyzed the influence of including a small amount of fluorescent absorbing particles to the nanocolloid of polystyrene nanospheres. Although the power to obtain the smallest size solitons was lower than the case of non-absorbing nanocolloid, we observed evidence of enhanced thermal effects affecting soliton stability. These instabilities are a consequence of the competition between the self-focusing effect, given by the nonlinear response of nanocolloid and self-defocusing which appears as an aftereffect of the heating of the sample for the presence of absorbing nanoparticles. Materials with this features become to be relevant nowadays, for example, metallic nanocolloids which presents plasmonic resonant effects can support stable ring propagation beams [83].

Finally, the most important contribution of this work was that incoherent soliton interactions were achieved experimentally for the first time in colloids with positive polarizability. We were able to observe two interaction regimes depending on two parameters: the interaction angle, and the power imbalance. The first regime was called steering because the two beams merge into a single one, and this can be continuously steered across the whole angular range by changing the relative power between the input beams. The second regime observed during soliton interactions lead to OSS switching. In this case the output can be switched between two limiting positions.The interaction angles used in this work go from $\gamma = 5°$ to $\gamma = 14°$, which is an order of magnitude bigger than the use with photorefractive crystals, which are in the order of 0.5°. [38].

The recent and ongoing development of artificial materials exhibiting novel optical properties has become one of the major scientific endeavors [2]. We can therefore conceive soft matter, such as nanocolloidal suspensions, as media with high potential to be efficiently engineered to open many photonic possibilities in the case of OSS formation and propagation.

Future work

Our results opened new questions about the nonlinear response of nanocolloidal suspensions and the properties of OSS in this media. Possible studies for future work are:

- In the case of Z-scan, a full description of the nonlinear phenomena observed in nanocolloids requires the development of a suitable theoretical model to properly fit the Z-scan curves, including the effects of nonlinear absorption and possibly non-locality which are present in dielectric nanocolloidal media. The known models of Z-scan are proposed for thin samples and consider absorption or non-locality separately. However, in this work we used thick samples (3 *mm*) in order to achieve similar experimental conditions to OSS formation experiments.

- The nonlinear optical response of dielectric nanocolloids might be improved with the new capabilities of nano-engineering. The efficiency can increase, for example, playing with the contrast between refractive index of the background and particles.

  Regarding to OSS formation and propagation we propose the following future investigations:

- The exploration of OSS formation with random laser emission within the colloid itself, using nanocolloids with fluorescent nanoparticles.

- Nowadays materials with a combination of sel-focusing and self-defocusing response have attracted great interest in the field of light-matter interaction due to their hability to form very stable OSS [83]. The colloids with a mixture of transparent and absorbing particles used in this work have the properties aforementioned. Is still missing to explore the optimal experimental conditions to allow the fluorescence guidance through OSS propagation path. In this

context an improvement of the visualization system is necessary in order to obtain well defined soliton propagation images, but also to demonstrate probe beam guidance.

- The soliton interaction observations open potentially rich scenarios for soliton-based optical steering and switching, and rapid response time of colloids suggest new application possibilities, for example to guide another beam through the solitons during interactions in order to build beam splitters or optical couplers in these media.

Appendices

Appendix A: Measurements of the cross-section and temporal stability of the OSS

The width of the cross-section of the OSS obtained in our experiments was estimated using video footage captured with the front-view system (see Fig.1 in chapter 2). The visualization system was focused inside the sample just behind the output end of the glass cell. Videos were acquired for each of the optical powers used to generate the OSS; they had a duration of 12.5 s and were composed of 300 frames. All the frames (Fig. A.1) were then used to evaluate the diameter of the cross-section of the beams exiting the cell following the methodology explained below.

Using a program made in Matlab, we were able to select the row with the highest intensity for each frame and then extract the intensity profile. The resulting profiles were fitted to a Gaussian curve and the fitting parameters yield beam features such as the width and the amplitude. Fig. A.2 shows a typical image analyzed to obtain the beam width. In this figure we can see three examples of the intensity profiles
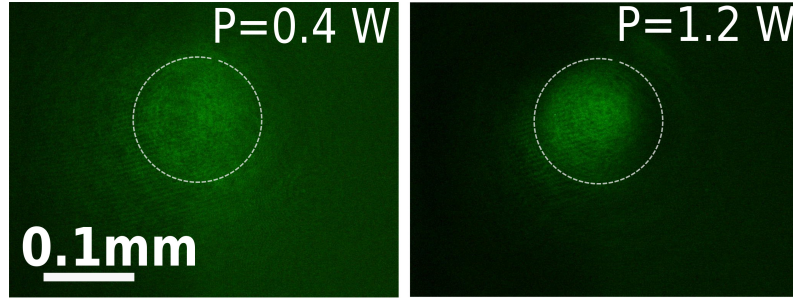
Figure A.1: Cross section beams images for $P = 0.4\ W$ (right) and $P = 1.2\ W$ (left). Dash line indicates the measure area.

a) and c) correspond to low power rows and and b) shows the maximum intensity row. The corresponding intensity profiles and the Gaussian fits are also shown in the figure.

The experimental points were fitted to the Gaussian curve given by:

$$I = a + (b - a)e^{-(\frac{x-c}{w})^2},\qquad\qquad\text{(A.1)}$$

In Eq. A.1 the parameter a is related to the amplitude, b to the y-position, c is the parameter related to x-position (see Fig. A.2 for the reference axes) and w is related to the width of the function. The latter was defined as the width of the Gaussian fit obtained when the amplitude decreases by $1/e$ of its maximum value (see Fig. A.2). This fitting process is repeated for each frame, and the beam width is then obtained averaging all the width values over all frames of the video. A few beam profiles and their corresponding fitted curves are illustrated in the Fig. A.3; in this case, the curve with the smallest amplitude represents an unstable soliton. In the footage, the instability appears as a change of the transversal size of the beam.
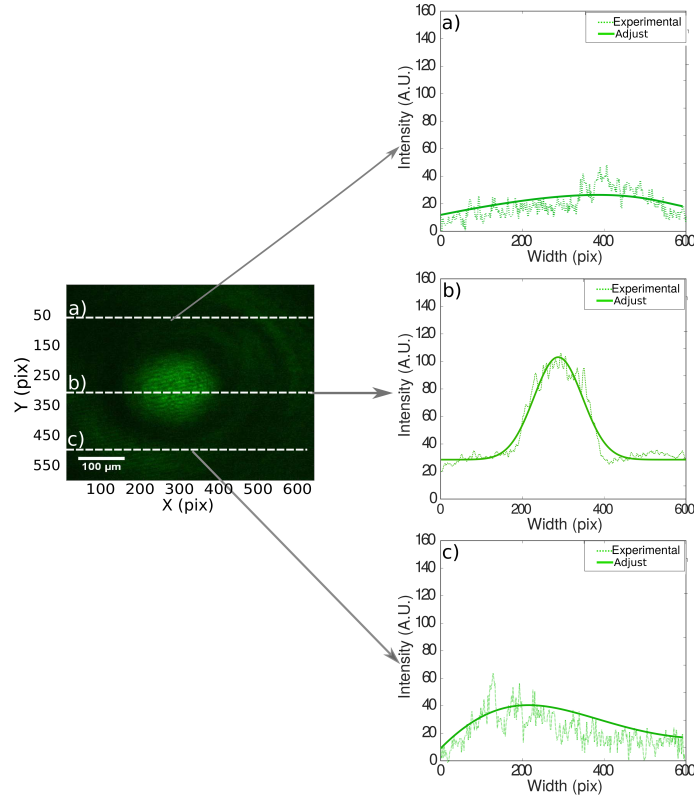
Figure A.2: Image of a soliton beam (left). As an example, the intensity profile and the Gaussian fitting are calculated for three rows in the image (marked with horizontal dashed lines). Rows *a*) and *c*) correspond to rows with low intensity and *b*) to the row with the maximum intensity.

Frames with deformation in the cross section circular shape were defined as "bad frames". In Fig. A.4 *a*) the cross section of a well formed soliton is shown, while in *b*) and *c*) examples of soliton deformations or "bad frames" are illustrated.

To discriminate the "bad frames" the following process was used: each video was indexed with letter j, the total number of videos was called nv. Then, each video was separated in frames (≈ 300), the frame index was i and the total number of frames was called Nim. Then, the histogram, h, of each frame was obtained and the program integrated the area under the curve to obtain its "magnitude"
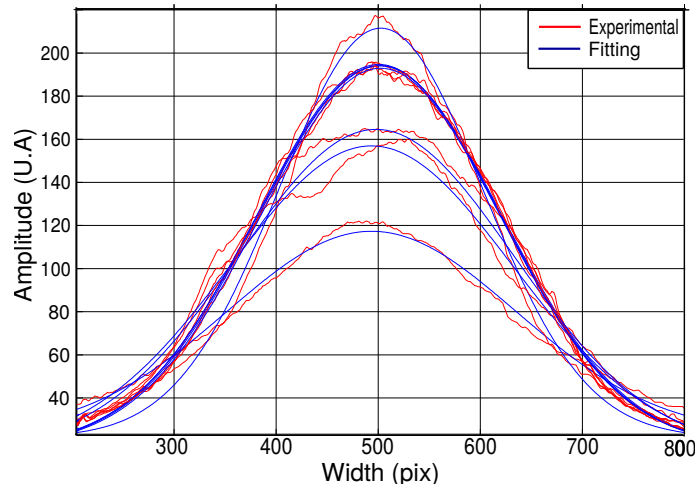
Figure A.3: Examples of experimental profiles of the image rows of maximum intensity (marked with dashed lines) and their respective adjusted Gaussian curves (continuous lines.

tH. The maximum value of the histogram magnitude was calculated and a normalization ($M = tH/Max(tH)$) was made. Once this process was completed for all frames the mode M was obtained and the discrimination condition of frames ($M < Mode(M) < 1$) was implemented. The frames satisfying this condition were processed as explained before, obtaining the maximum intensity row and fit a Gaussian curve which gives the width parameter corresponding to the diameter w of the beam. A flow chart illustrating this process is shown in Fig.A.5

The identification of the bad frames further provides a means to observe the evolution of the beam with time. This was done through a "temporal evolution program," which plots the beam profile over time. In this case, the program read each video (j), and splited it into frames ($\approx 170\ frames$, $\approx 2.5\ s$). Each frame corresponded to a specific time and the program found the column with maximum pixel intensity and fixed that position, then the corresponding row was identified and the intensity

Figure A.4: Profiles of the soliton instabilities and their corresponding pictures, dashed horizontal lines indicate the rows of which the corresponding profile was obtained. The three pictures belong to the same video at different times. a) A well formed soliton ($t = 0.6$ s), b) insatiability of the beam ($t = 1.5$ s), the width is bigger respect to a), and c) other instability instant ($t = 6.5$ s).

profile (Ii) was plotted and saved. When all frames were analyzed the plot of all Ii *vs t* was made creating a 2D image of the temporal evolution of the beam. At the end of the analysis, the pixels were converted to microns using a standard reference scale. A typical plot for temporal evolution analysis is shown in Fig. A.6 and the flow chart for the program is shown in Fig. A.7. This analysis provides information about the soliton dynamics; it is particularly useful indicating OSS temporal instabilities.
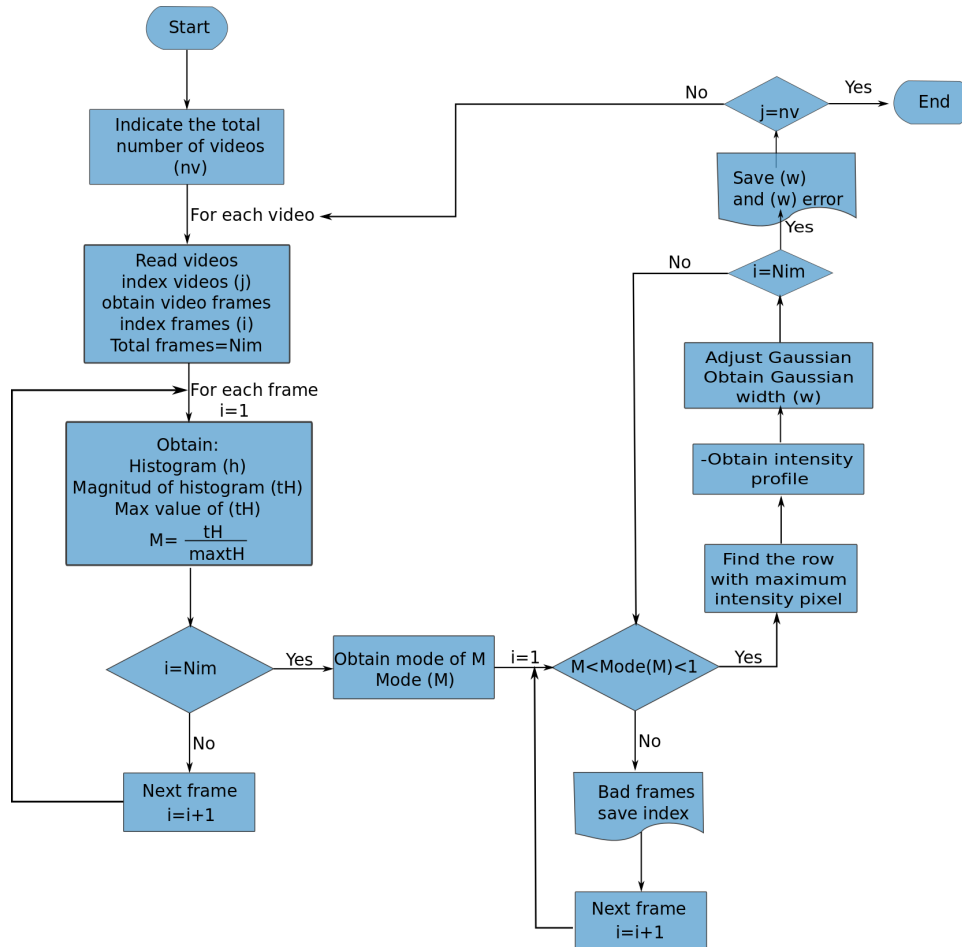
Figure A.5: Flow diagram of the implemented program to obtain the beam width, nv indicates the total number of videos, Nim the total number of frames, j is the video index, i frames index, h is the histogram, tH the maximum value of the histogram, M normalization of tH and w indicates the Gaussian fit width.
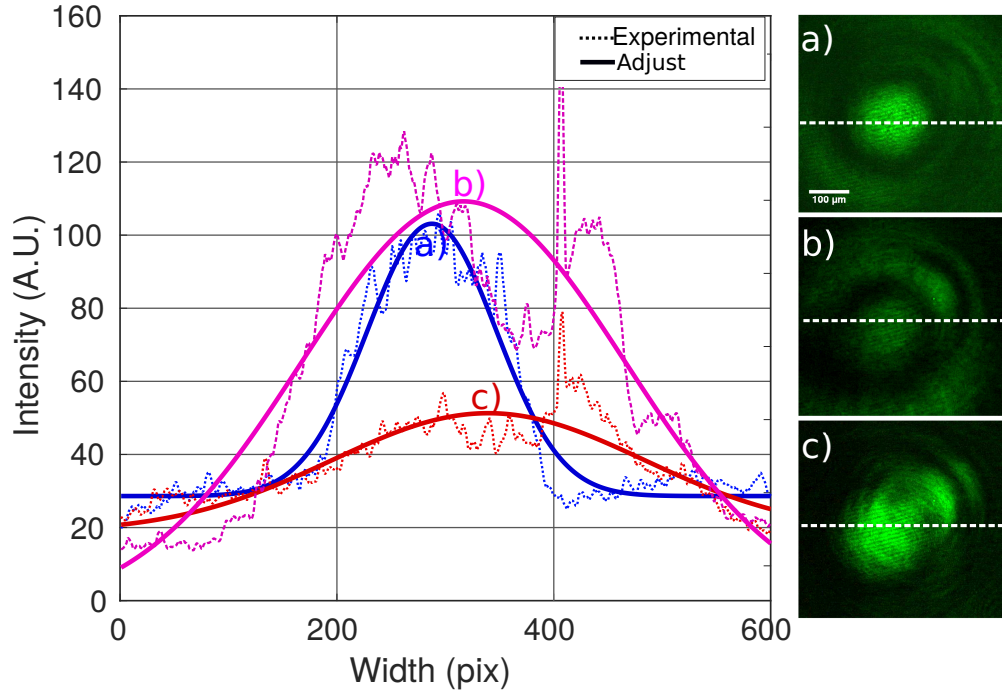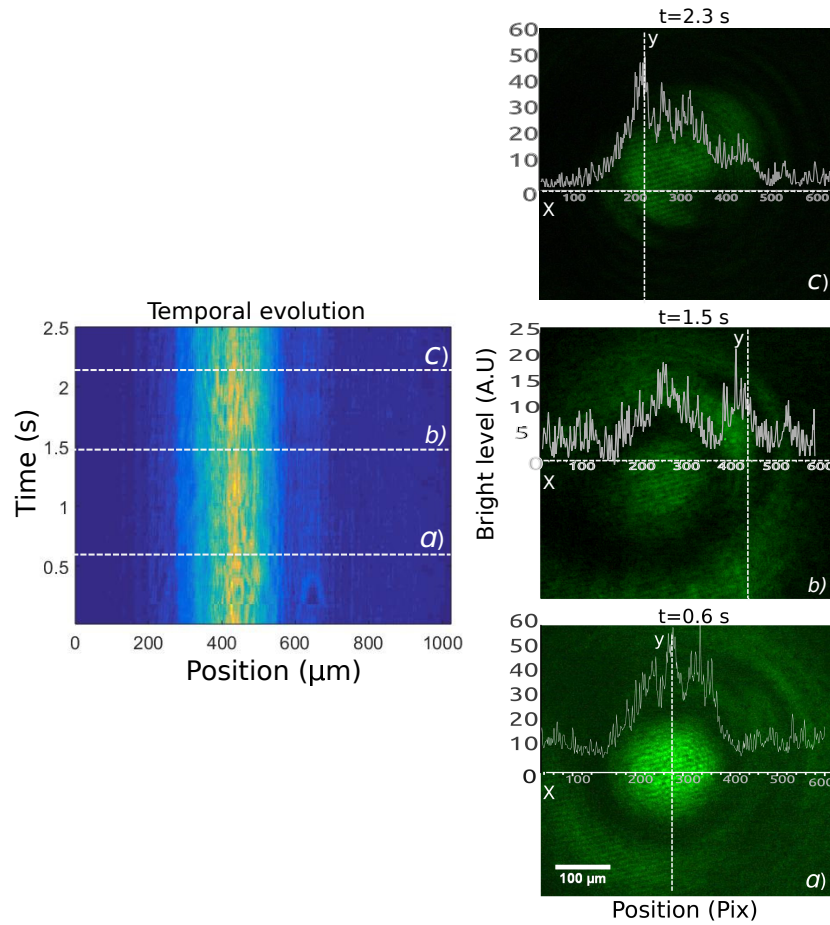
Figure A.6: Profiles of the soliton *a*), its instabilities *b*), *c*) and their corresponding pictures, dashed horizontal lines indicate the rows of the corresponding profile. The three pictures belong to the same video at different times. a) A well formed soliton ($t = 0.6$ *s*), b) insatiability of the beam ($t = 1.5$ and $t = 2.3$ *s*). Image on the left is an example of a temporal evolution of a soliton of the suspension with 62 *nm* particles at 0.93 *W* of incident power.
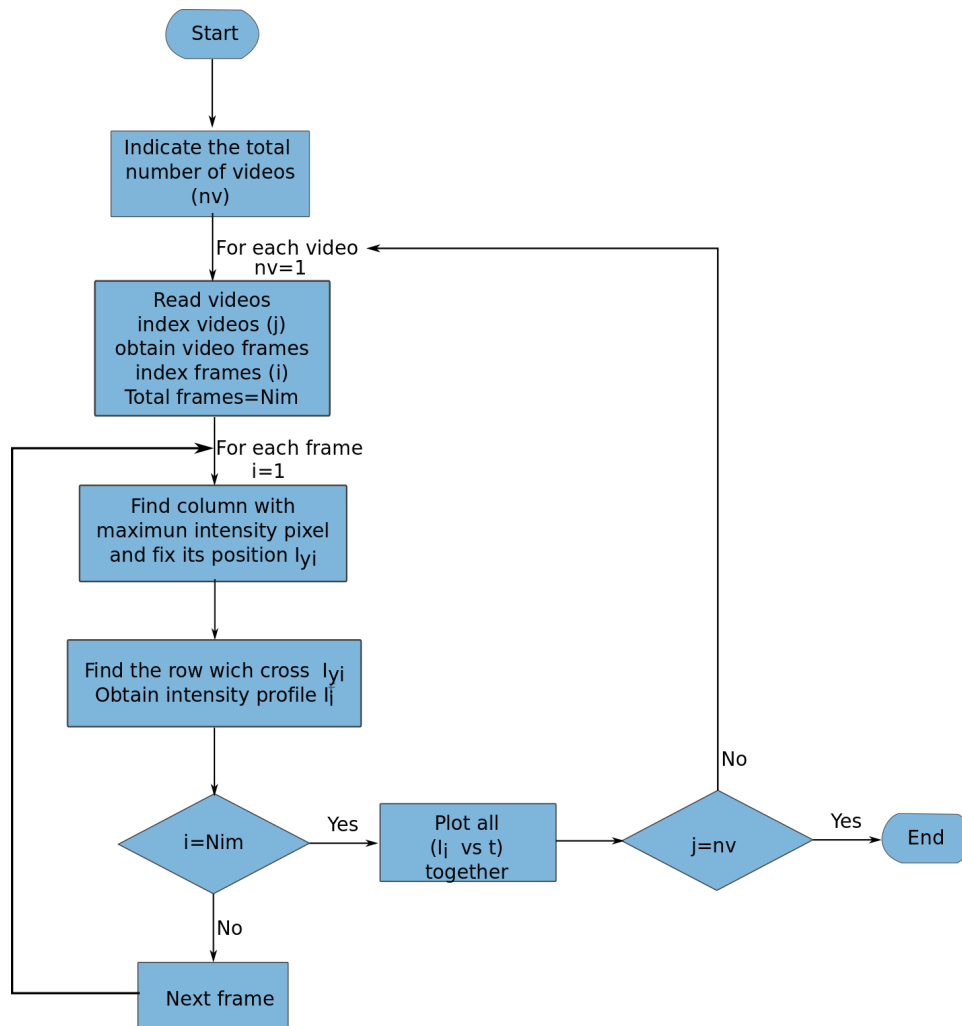
Figure A.7: Process to create the images for temporal evolution of an OSS, a) defined cross section of a OSS and the intensity profile, b) bad frame an its profile, c) temporal evolution of an OSS along 2.5 s. nv indicates the total number of videos, Nim the total number of frames, j is the video index, i frames index, Iy_i indicates the maximum intensity pixel, I_j indicates, the intensity profile and t the time.

Appendix B: Theoretical model of soliton interactions

In order to model our experiments, we follow Ref. [29] for describing soliton propagation in a colloid with dielectric nanoparticles interacting via a hard-sphere potential and neglecting scattering losses. The slowly-varying envelope of the electric field of each beam in the medium, u_j $(j = 1, 2)$, satisfies

$$i\frac{\partial u_j}{\partial \tilde{z}} + \frac{1}{2}\frac{A}{B^2}\nabla_\perp{}^2 u_j + (\eta - \eta_0)C u_j = 0, \tag{B.1}$$

$$|u_1|^2 = \frac{Q\alpha\beta}{4C^2}|E|^2; \quad |u_2|^2 = \frac{(1 - Q)\alpha\beta}{4C^2}|E|^2, \tag{B.2}$$

where $0 \leq Q \leq 1$ indicates the power balance between the beams, $\tilde{z}$ is a dimensionless propagation coordinate and $\nabla_\perp{}^2$ acts on the dimensionless coordinates $(\tilde{x}, \tilde{y})$. A, B and C are constants related to a rescaling based on the width of the self-collimated beam. The polarizability of the colloid is $\alpha = 3V_p\epsilon_0 n_b^2\delta$, with $\delta = (m^2 - 1)/(m^2 + 2)$ and $m = n_p/n_b$; V_p is the particle volume, ϵ_0 the vacuum electric permittivity and $\beta^{-1} = k_B T$, with T the temperature of the liquid and k_B

the Boltzmann constant. $I = c\epsilon_0 n_b |E|^2/2$ is the intensity, c is the speed of light in vaccuum and E the electric field. The nonlinear response of the medium is given by [29]: $g(\eta) - g(\eta_0) = C^2 \left(|u_1|^2 + |u_2|^2\right)$, where $g(\eta) = \ln \eta + (3-\eta)/(1-\eta)^3$; η and η_0 are the packing fraction of the colloid in presence and absence of the light field, respectively. The interaction is introduced at the input boundary, by considering that each beam enters the medium with an inclination of $\pm\gamma/2$ with respect to the z axis.

Bibliography

[1] A. Ashkin, J. Dziedzic, and P. Smith, "Continuous-wave self-focusing and self-trapping of light in artificial kerr media," *Optics letters*, vol. 7, no. 6, pp. 276–278, 1982.

[2] W. Man, S. Fardad, Z. Zhang, J. Prakash, M. Lau, P. Zhang, M. Heinrich, D. N. Christodoulides, and Z. Chen, "Optical nonlinearities and enhanced light transmission in soft-matter systems with tunable polarizabilities," *Physical review letters*, vol. 111, no. 21, p. 218302, 2013.

[3] K. Birdi and S. , *Handbook of surface and colloid chemistry.* CRC press, 2002.

[4] F. Evers, R. Hanes, C. Zunke, R. Capellmann, J. Bewerunge, C. Dalle-Ferrier, M. Jenkins, I. Ladadwa, A. Heuer, R. Castañeda-Priego, *et al.*, "Colloids in light fields: Particle dynamics in random and periodic energy landscapes," *The European Physical Journal Special Topics*, vol. 222, no. 11, pp. 2995–3009, 2013.

[5] R. W. Boyd, *Nonlinear optics.* Elsevier, 2003.

[6] B. E. Saleh, M. C. Teich, and B. E. Saleh, *Fundamentals of photonics*, vol. 22. Wiley New York, 1991.

[7] Y. S. Kivshar and G. Agrawal, *Optical solitons: from fibers to photonic crystals.* Academic press, 2003.

[8] R. A. Terborg, J. P. Torres, and K. Volke-Sepulveda, "Steering and guiding light with light in a nanosuspension," *Optics letters*, vol. 38, no. 24, pp. 5284–5287, 2013.

[9] M. Y. Salazar-Romero, Y. A. Ayala, E. Brambila, L. A. Lopez-Peña, L. Sciberras, A. A. Minzoni, R. A. Terborg, J. P. Torres, and K. Volke-Sepúlveda, "Steering and switching of soliton-like beams via interaction in a nanocolloid with positive polarizability," *Optics letters*, vol. 42, no. 13, pp. 2487–2490, 2017.

[10] R. L. Byer, "Nonlinear optical phenomena and materials," *Annual Review of Materials Science*, vol. 4, no. 1, pp. 147–190, 1974.

[11] Y.-R. Shen, "The principles of nonlinear optics," *New York, Wiley-Interscience, 1984, 575 p.*, 1984.

[12] D. L. Mills, *Nonlinear optics: basic concepts.* Springer Science & Business Media, 2012.

[13] J. Wei, *Nonlinear super-resolution nano-optics and applications.* Springer, 2015.

[14] M. Segev, "Optical spatial solitons," *Optical and Quantum Electronics*, vol. 30, no. 7-10, pp. 503–533, 1998.

[15] G. I. Stegeman and M. Segev, "Optical spatial solitons and their interactions:

universality and diversity," *Science*, vol. 286, no. 5444, pp. 1518–1523, 1999.

[16] R. Gordon, J. Blakely, and D. Sinton, "Particle-optical self-trapping," *Physical Review A*, vol. 75, no. 5, p. 055801, 2007.

[17] B. Crosignani and G. Salamo, "Photorefractive solitons," *Optics and Photonics News*, vol. 13, no. 2, pp. 38–41, 2002.

[18] G. Assanto, *Nematicons: Spatial Optical Solitons in Nematic Liquid Crystals*, vol. 74. John Wiley & Sons, 2012.

[19] M. Peccianti, A. De Rossi, G. Assanto, A. De Luca, C. Umeton, and I. Khoo, "Electrically assisted self-confinement and waveguiding in planar nematic liquid crystal cells," *Applied Physics Letters*, vol. 77, no. 1, pp. 7–9, 2000.

[20] J. W. Goodwin and R. H. Ottewill, "Properties of concentrated colloidal dispersions," *Journal of the Chemical Society, Faraday Transactions*, vol. 87, no. 3, pp. 357–369, 1991.

[21] J. Mewis and N. J. Wagner, *Colloidal suspension rheology*. Cambridge University Press, 2012.

[22] H. N. Lekkerkerker and R. Tuinier, *Colloids and the depletion interaction*, vol. 833. Springer, 2011.

[23] P. Smith, A. Ashkin, and W. Tomlinson, "Four-wave mixing in an artificial kerr medium," *Optics letters*, vol. 6, no. 6, pp. 284–286, 1981.

[24] P. Smith, P. Maloney, and A. Ashkin, "Use of a liquid suspension of dielectric spheres as an artificial kerr medium," *Optics letters*, vol. 7, no. 8, pp. 347–349, 1982.

[25] P. Smith, A. Ashkin, J. E. Bjorkholm, and D. Eilenberger, "Studies of self-focusing bistable devices using liquid suspensions of dielectric particles," *Optics letters*, vol. 9, no. 4, pp. 131–133, 1984.

[26] S. Fardad, A. Salandrino, M. Heinrich, P. Zhang, Z. Chen, and D. N. Christodoulides, "Plasmonic resonant solitons in metallic nanosuspensions," *Nano letters*, vol. 14, no. 5, pp. 2498–2504, 2014.

[27] C. Conti, G. Ruocco, and S. Trillo, "Optical spatial solitons in soft matter," *Physical review letters*, vol. 95, no. 18, p. 183902, 2005.

[28] R. El-Ganainy, D. Christodoulides, C. Rotschild, and M. Segev, "Soliton dynamics and self-induced transparency in nonlinear nanosuspensions," *Optics express*, vol. 15, no. 16, pp. 10207–10218, 2007.

[29] M. Matuszewski, W. Krolikowski, and Y. S. Kivshar, "Spatial solitons and light-induced instabilities in colloidal media," *Optics express*, vol. 16, no. 2, pp. 1371–1376, 2008.

[30] R. El-Ganainy, D. N. Christodoulides, E. Wright, W. Lee, and K. Dholakia, "Nonlinear optical dynamics in nonideal gases of interacting colloidal nanoparticles," *Physical Review A*, vol. 80, no. 5, p. 053805, 2009.

[31] M. Matuszewski, "Engineering optical soliton bistability in colloidal media," *Physical Review A*, vol. 81, no. 1, p. 013820, 2010.

[32] W. Lee, R. El-Ganainy, D. Christodoulides, K. Dholakia, and E. Wright, "Nonlinear optical response of colloidal suspensions," *Optics Express*, vol. 17, no. 12, pp. 10277–10289, 2009.

[33] Y. S. Kivshar and G. I. Stegeman, "Spatial optical solitons," *Optics and Photonics News*, vol. 13, no. 2, pp. 59–63, 2002.

[34] M. Peccianti, C. Conti, G. Assanto, A. De Luca, and C. Umeton, "Routing of anisotropic spatial solitons and modulational instability in liquid crystals," *Nature*, vol. 432, no. 7018, p. 733, 2004.

[35] R. Barboza, A. Alberucci, and G. Assanto, "Large electro-optic beam steering with nematicons," *Optics letters*, vol. 36, no. 14, pp. 2725–2727, 2011.

[36] M. Peccianti and G. Assanto, "Nematicons," *Physics Reports*, vol. 516, no. 4-5, pp. 147–208, 2012.

[37] Y. V. Izdebskaya, V. G. Shvedov, A. S. Desyatnikov, W. Krolikowski, and Y. S. Kivshar, "Soliton bending and routing induced by interaction with curved surfaces in nematic liquid crystals," *Optics letters*, vol. 35, no. 10, pp. 1692–1694, 2010.

[38] A. Mamaev, M. Saffman, and A. Zozulya, "Phase-dependent collisions of (2+1)-dimensional spatial solitons," *JOSA B*, vol. 15, no. 7, pp. 2079–2082, 1998.

[39] G. McCarthy, T. Breuninger, J. Schröder, C. Denz, D. Neshev, and W. Krolikowski, "Mutual spatial-soliton trapping in photorefractive media: experiment versus theory," *Applied Physics B*, vol. 77, no. 4, pp. 421–426, 2003.

[40] Z. Chen, M. Segev, and D. N. Christodoulides, "Optical spatial solitons: historical overview and recent advances," *Reports on Progress in Physics*, vol. 75, no. 8, p. 086401, 2012.

[41] Y. V. Izdebskaya, J. Rebling, A. Desyatnikov, G. Assanto, and Y. S. Kivshar, "All-optical switching of a signal by a pair of interacting nematicons," *Optics express*, vol. 20, no. 22, pp. 24701–24707, 2012.

[42] M. Peccianti, K. A. Brzdąkiewicz, and G. Assanto, "Nonlocal spatial soliton interactions in nematic liquid crystals," *Optics letters*, vol. 27, no. 16, pp. 1460–1462, 2002.

[43] M. Matuszewski, W. Krolikowski, and Y. S. Kivshar, "Soliton interactions and transformations in colloidal media," *Physical Review A*, vol. 79, no. 2, p. 023814, 2009.

[44] S. Fardad, M. S. Mills, P. Zhang, W. Man, Z. Chen, and D. Christodoulides, "Interactions between self-channeled optical beams in soft-matter systems with artificial nonlinearities," *Optics letters*, vol. 38, no. 18, pp. 3585–3587, 2013.

[45] T. Cosgrove, *Colloid science: principles, methods and applications*. John Wiley & Sons, 2010.

[46] U.-v. Technique, "*https : //www.mri.psu.edu/materials − characterization − lab/characterization − techniques/ultraviolet − visible − spectroscopy − uv − vis*," April 2018.

[47] M. Gaft, R. Reisfeld, and G. Panczer, *Modern luminescence spectroscopy of minerals and materials.* Springer, 2015.

[48] G. I. Stegeman and R. A. Stegeman, *Nonlinear optics: phenomena, materials and devices*, vol. 78. John Wiley & Sons, 2012.

[49] G. Fibich and A. L. Gaeta, "Critical power for self-focusing in bulk media and in hollow waveguides," *Optics letters*, vol. 25, no. 5, pp. 335–337, 2000.

[50] I. Severiano Carrillo, M. M. Méndez Otero, M. L. Arroyo Carrasco, and M. D. Iturbe Castillo, "Comparison of different models employed to describe the z-scan curves for thick nonlinear optical media," *Journal of Modern Optics*, vol. 60, no. 3, pp. 248–254, 2013.

[51] M. Sheik-Bahae, A. A. Said, T.-H. Wei, D. J. Hagan, and E. W. Van Stryland, "Sensitive measurement of optical nonlinearities using a single beam," *IEEE journal of quantum electronics*, vol. 26, no. 4, pp. 760–769, 1990.

[52] T. Wei, D. Hagan, M. Sence, E. Van Stryland, J. Perry, and D. Coulter, "Direct measurements of nonlinear absorption and refraction in solutions of phthalocyanines," *Applied Physics B*, vol. 54, no. 1, pp. 46–51, 1992.

[53] M. Sheik-Bahae, A. A. Said, and E. W. Van Stryland, "High-sensitivity, single-

beam n 2 measurements," *Optics letters*, vol. 14, no. 17, pp. 955–957, 1989.

[54] Q.-F. Dai, H.-Y. Liu, J. Liu, L.-J. Wu, Q. Guo, W. Hu, X.-B. Yang, S.-H. Liu, S. Lan, A. V. Gopal, *et al.*, "Self-induced transparency in colloidal liquids by z-scan-based optical trapping," *Applied Physics Letters*, vol. 92, no. 15, p. 153111, 2008.

[55] J. G. Mercado-Vásquez, "Automatización de la técnica z-scan y su aplicación al estudio del índice de refracción no lineal y el coeficiente de absorción de tercer orden en películas de pmma contaminadas con dr1," Junio 2015.

[56] J. Gordon, R. Leite, R. Moore, S. Porto, and J. Whinnery, "Long-transient effects in lasers with inserted liquid samples," *Journal of Applied Physics*, vol. 36, no. 1, pp. 3–8, 1965.

[57] C. A. Carter and J. M. Harris, "Comparison of models describing the thermal lens effect," *Applied optics*, vol. 23, no. 3, pp. 476–481, 1984.

[58] C. Hu and J. Whinnery, "New thermooptical measurement method and a comparison with other methods," *Applied optics*, vol. 12, no. 1, pp. 72–79, 1973.

[59] E. R. Lara, Z. N. Meza, M. D. I. Castillo, C. G. T. Palacios, E. M. Panameño, and M. L. A. Carrasco, "Influence of the photoinduced focal length of a thin nonlinear material in the z-scan technique," *Optics express*, vol. 15, no. 5, pp. 2517–2529, 2007.

[60] M. Segev, "Self-trapping of optical beams: spatial solitons," *Phys. Today*,

vol. 51, pp. 42–48, 1998.

[61] O. Bang, W. Krolikowski, J. Wyller, and J. J. Rasmussen, "Collapse arrest and soliton stabilization in nonlocal nonlinear media," *Physical Review E*, vol. 66, no. 4, p. 046619, 2002.

[62] P. H. Jones, O. M. Maragò, and G. Volpe, *Optical tweezers: Principles and applications.* Cambridge University Press, 2015.

[63] A. Ashkin, "Forces of a single-beam gradient laser trap on a dielectric sphere in the ray optics regime," *Biophysical journal*, vol. 61, no. 2, pp. 569–582, 1992.

[64] A. Ashkin, *Optical trapping and manipulation of neutral particles using lasers: a reprint volume with commentaries.* World Scientific, 2006.

[65] M. Matuszewski, W. Krolikowski, and Y. S. Kivshar, "Spatial solitons and light-induced instabilities in colloidal media," *Optics express*, vol. 16, no. 2, pp. 1371–1376, 2008.

[66] *Bangs Laboratories*, March 2015.

[67] R. G. Kadhim, "Study of some optical properties of polystyrene-copper nanocomposite films," *World Scientific News*, no. 30, pp. 14–25, 2016.

[68] E. G. Ramirez, M. A. Carrasco, M. M. Otero, E. R. Lara, S. Chavez-Cerda, and M. I. Castillo, "Z-scan and spatial self-phase modulation of a gaussian beam in a thin nonlocal nonlinear media," *Journal of optics*, vol. 13, no. 8, p. 085203,

2011.

[69] A. B. Ortega, M. A. Carrasco, M. M. Otero, E. R. Lara, E. G. Ramírez, and M. I. Castillo, "Analytical expressions for z-scan with arbitrary phase change in thin nonlocal nonlinear media," *Optics express*, vol. 22, no. 23, pp. 27932–27941, 2014.

[70] M. Braibanti, D. Vigolo, and R. Piazza, "Does thermophoretic mobility depend on particle size?," *Physical review letters*, vol. 100, no. 10, p. 108303, 2008.

[71] M. Gorkunov, E. Podivilov, and B. Sturman, "Critical enhancement of nonlinear response in fast photorefractive crystals," *Journal of Experimental and Theoretical Physics*, vol. 94, no. 3, pp. 470–481, 2002.

[72] Y. Lamhot, A. Barak, O. Peleg, and M. Segev, "Self-trapping of optical beams through thermophoresis," *Physical review letters*, vol. 105, no. 16, p. 163906, 2010.

[73] G. Swartzlander Jr, D. Andersen, J. Regan, H. Yin, and A. Kaplan, "Spatial dark-soliton stripes and grids in self-defocusing materials," *Physical review letters*, vol. 66, no. 12, p. 1583, 1991.

[74] B. Luther-Davies and Y. Xiaoping, "Waveguides and y junctions formed in bulk media by using dark spatial solitons," *Optics letters*, vol. 17, no. 7, pp. 496–498, 1992.

[75] S. Perumbilavil, A. Piccardi, R. Barboza, O. Buchnev, M. Kauranen,

G. Strangi, and G. Assanto, "Beaming random lasers with soliton control," *Nature communications*, vol. 9, no. 1, p. 3863, 2018.

[76] Inkscape, "http://www.littlewebhut.com/inkscape/graphics_filter_guide," May 2018.

[77] D. Träger, A. Strinić, J. Schröder, C. Denz, M. Belić, M. Petrović, S. Matern, and H. Purwins, "Interactions in large arrays of solitons in photorefractive crystals," *Journal of Optics A: Pure and Applied Optics*, vol. 5, no. 6, p. S518, 2003.

[78] J. Gordon, "Interaction forces among solitons in optical fibers," *Optics letters*, vol. 8, no. 11, pp. 596–598, 1983.

[79] D. Anderson and M. Lisak, "Bandwidth limits due to incoherent soliton interaction in optical-fiber communication systems," *Physical Review A*, vol. 32, no. 4, p. 2270, 1985.

[80] M. Peccianti, K. A. Brzdąkiewicz, and G. Assanto, "Nonlocal spatial soliton interactions in nematic liquid crystals," *Optics letters*, vol. 27, no. 16, pp. 1460–1462, 2002.

[81] M. Matuszewski, "Engineering optical soliton bistability in colloidal media," *Physical Review A*, vol. 81, no. 1, p. 013820, 2010.

[82] S. Fardad, M. S. Mills, P. Zhang, W. Man, Z. Chen, and D. Christodoulides, "Interactions between self-channeled optical beams in soft-matter systems with

artificial nonlinearities," *Optics letters*, vol. 38, no. 18, pp. 3585–3587, 2013.

[83] V. Shvedov, K. Cyprych, M. Y. Salazar-Romero, Y. Izdebskaya, and W. Krolikowski, "Nonlinear propagation and quasi self-confinement of light in plasmonic resonant media," *Optics express*, vol. 26, no. 18, pp. 23196–23206, 2018.